

**TOWARDS RESOLVED-SIDEBAND
RAMAN COOLING OF A SINGLE ^{87}Rb
ATOM IN A FORT**

LEE JIANWEI

NATIONAL UNIVERSITY OF SINGAPORE

2010

**TOWARDS RESOLVED-SIDEBAND
RAMAN COOLING OF A SINGLE ^{87}Rb
ATOM IN A FORT**

LEE JIANWEI

B. Phy. (Hons.), NUS

**A THESIS SUBMITTED
FOR THE DEGREE OF MASTER OF SCIENCE**

**DEPARTMENT OF PHYSICS
NATIONAL UNIVERSITY OF SINGAPORE**

**SINGAPORE
2010**

Acknowledgements

First thanks goes foremost to my parents, who are the wind beneath my wings, whose love language is to feed and maintain me everyday without complaining, and being willing to travel all the way to Changi to get me a laptop dc power supply, despite the fact that I spend most of my time out of home.

Special thanks goes to Christian Kurtsiefer, my research advisor, who proofread the thesis drafts, taught me quantum optics, electronics and exposing me to conferences that I didn't think I fully deserved to go.

Thanks to Gleb Maslennikov, before whom I've never met a real-life Russian but now I find them very amusing. He's taught me about cavities, milling, lathing, girls, chocolates and vodka; a competent experimental physicist and a patient mentor.

Thanks to Syed Abdullah Aljunid who has been indispensable to the quantum optics team. His proficiency in almost every experimental equipment and technique, from atomic physics to optics to hardware to programming to troubleshooting to turning knobs near the edge of human sensitivity, has been a great testimony to what patience and common sense can do. Thanks for staying up as long as I have for the experiments and also giving me free

rides home.

Thanks to Brenda Chng who went through the pain of reading the longest equations in the appendix, coaching me in electronics and getting beef noodles. Thanks to Dingyuan for proofreading the draft. Thanks to Martin Paesold who fleshed out the wavemeter controller-thoroughly enjoyed your company. Thanks to Dao Hoang Lan for helping me out with the fried laser controller. Thanks to Chang who said the most amusing statement to an advisor during a group meeting ‘would you like to listen to last week’s problems or to new problems?’. Thanks to Ho Shun, Tien Tjun and Siddarth who taught me optics and electronics, amongst other things. Thanks also to Valerio Scarani, Timothy Liew and Colin Teo for the discussions regarding the release and recapture experiment and also the temperature dependence of the probe extinction experiment.

Of course, there are many more people who have helped make all this possible: Chin Pei Pei our procurement manager; the machine workshop guys from the physics department, Eng Swee, Uncle Bob and Jovan who helped with electronics and milling the cavity body respectively... it’s impossible to name everyone!

Final thanks goes to the Friend who was my constant companion during the quiet nights when even the best of friends have returned home.

Contents

| | |
|---|-----------|
| Acknowledgements | i |
| Summary | vi |
| 1 Introduction | 1 |
| 2 Trapping and interrogating a single atom | 4 |
| 2.1 Experimental Setup | 4 |
| 2.1.1 Magneto Optical Trap | 6 |
| 2.1.2 Far off-resonant dipole trap (FORT) | 8 |
| 2.2 Extinction Experimental Sequence | 11 |
| 2.3 Conclusions of Extinction Experiment | 15 |
| 3 Energy distribution of a single atom in the FORT | 17 |
| 3.1 Release-recapture experimental sequence | 18 |
| 3.2 Extracting the temperature | 21 |
| 3.3 Results | 24 |
| 3.4 Discussion | 25 |
| 3.4.1 Comparison with Probe extinction | 25 |

| | | |
|----------|---|-----------|
| 3.4.2 | Validity of classical treatment | 27 |
| 4 | Towards resolved-sideband Raman Cooling | 28 |
| 4.1 | Background | 28 |
| 4.1.1 | Sub-Doppler cooling in the FORT | 29 |
| 4.1.2 | Sub-Recoil cooling in the FORT | 31 |
| 4.1.3 | Choice of cooling transition | 33 |
| 4.2 | Sideband Cooling Setup | 34 |
| 4.2.1 | Main Laser | 34 |
| 4.2.2 | Creating the Raman beams | 35 |
| 4.3 | Resolved-sideband Raman Cooling Cycle in ^{87}Rb | 40 |
| 4.4 | Coherence time measurements | 42 |
| 4.4.1 | Rabi oscillation | 43 |
| 4.4.2 | Results | 46 |
| 4.4.3 | Increasing coherence time | 46 |
| 4.5 | Outlook | 50 |
| | Conclusion | 52 |
| | Bibliography | 57 |
| A | | 61 |
| A.1 | The D1 and D2 transition hyperfine structure of the ^{87}Rb atom | 61 |
| A.2 | FORT characteristics | 62 |
| A.2.1 | AC Stark shift | 62 |
| A.2.2 | Trap Frequencies | 68 |
| A.2.3 | FORT Scattering Rate | 69 |

| | |
|--|----|
| A.3 Average vibrational quantum number in FORT | 70 |
| A.4 Two-photon stimulated Raman transitions and motional state coupling | 72 |

Summary

In the work presented here, we perform an experiment to determine the energy distribution of an ensemble of single ^{87}Rb atoms localised in a strongly focused far off-resonant optical dipole trap (FORT). The trapped atom is optically cooled to a temperature below the Doppler temperature ($< 144 \mu\text{K}$), and optically pumped into a two-level cycling transition. An atom prepared in this manner interacts strongly with a weak coherent light beam tightly focused by a lens [1]. The measured energy distribution will reveal if its oscillatory motion was the cause of decreased extinction of a strongly focused probe in a previous experiment, where the measured extinction was 10.4%, compared to the theoretical prediction of over 20% [2]. We follow the capture and release method of Grangier et al. [3], whereby the FORT was switched off for a variable time, allowing the atom to fall under gravity. We detect if it was recaptured by the FORT when the trap restarts. Repeating the experiment above for an ensemble allows us to determine the probability of recapture, dependent on release time and ensemble energy distribution. Fitting the experimental data with a simulation that treated the atom's trajectory in the FORT classically, yielded an ensemble energy distribution characterised by a temperature $T = 35 \mu\text{K}$, which we determine to be too small to account

for the 50% reduction of extinction. We thus exclude the initial temperature distribution as the only cause for this reduction.

We also investigate the feasibility of performing sideband-resolved Raman cooling on the atom in order to bring it to the vibrational ground state of the FORT. An experiment was set up to perform this cooling scheme. The two-photon Raman transition between two hyperfine ground states was driven. Within this project a coherence time of $3.3\ \mu\text{s}$ was observed – this is too short for the Raman pulses to resolve the trap frequencies at 80 kHz and 13 kHz required for the proposed cooling technique. To increase coherence time, an alternate scheme utilising magnetically insensitive Zeeman states is suggested.

Chapter 1

Introduction

Several quantum information protocols require strong interaction between light and matter in order to transmit and store quantum states of light between a sender and a receiver, or between nodes in a quantum network [4, 5, 6, 7, 8, 9]. This is because one cannot perform a measurement on the quantum state of matter at one node and transfer the information classically to another node (no-cloning theorem). However, a coherent interaction between light and matter allows the transfer of quantum information between two nodes. Such a system has been realised [4, 10, 11, 12, 13, 14] using photons as the ‘quantum channel’, while the sending and receiving nodes are formed by trapped atoms or ions.

One approach to achieve strong atom-photon interaction is to place the atom within a high-finesse cavity, in which the electrical field strength is enhanced by multiple reflections between two highly reflective mirrors thus resulting in a higher absorption probability of the photon [10, 15, 13, 14]. Alternatively, Tey et al [1] recently achieved strong extinction (10.4%) of a

weak coherent beam by a single ^{87}Rb atom in a FORT by strongly focusing the beam. This is motivated by the fact that for an atom, its absorption cross-section is on the order of the square of the interacting optical wavelength and not the size of the electron orbital [16]. Thus by focusing the interacting beam down to a diffraction-limited spot (whose spot size is also of the order of the squared of the optical wavelength) on a well-localised atom in a FORT, a huge percentage of the field can be absorbed and re-scattered on a single pass [17]. This new approach is worth further study because as opposed to a high-finesse cavity, a lens system is relatively easier to setup.

However, in a real scenario, the atom carries some residual kinetic energy and so it oscillates about the location where the field strength of the interacting beam is the maximum. Thus the time-averaged scattering rate of the beam is reduced. It was estimated [2] that for an ensemble of single atoms similarly trapped and Doppler-cooled in the FORT, with a Maxwell-Boltzmann energy distribution characterised by a temperature parameter $T = 100 \mu\text{K}$, the residual kinetic energy caused the scattering rate to reduce by $\sim 20\%$. The remaining $\sim 30\%$ in reduction of the scattering rate ¹ was attributed to other factors [2], such as imperfections in the focusing apparatus. As $T = 100 \mu\text{K}$ used in this analysis was arbitrarily chosen ², we aim to experimentally determine its value in this work. To approach the theoret-

¹A 50% reduction in scattering rate of the interacting beam was observed between the theoretical and measured values. The theoretical value was determined based on a stationary atom in the FORT.

²In the FORT, the atom undergoes laser cooling at the cooling transition $|5S_{1/2}, F = 2\rangle \rightarrow |5P_{3/2}, F' = 3\rangle$. The cooling method ‘Doppler cooling’ [16] has a lower limit to the lowest possible temperature attainable and can be shown to be $T_{dopp} = 144 \mu\text{K}$. It is however possible that the actual temperature is lower than T_{dopp} due to an additional cooling mechanism ‘sub-Doppler’ cooling (see Section 4.1.1) not taken into account by Doppler cooling theory. Thus, an order-of-magnitude value for T was chosen to be $100 \mu\text{K}$.

ical extinction limit, we setup the apparatus to implement a more effective cooling technique, to approach the vibrational ground state of the trapping potential.

The organisation of this thesis is as follows: In Chapter 2 we introduce the trap in the Tey [2] extinction experiment. In Chapter 3 we present the experiment which parametrises the energy distribution of an ensemble of single atoms in this trap by the ensemble temperature T . A calculation illustrating the dependence of extinction with T , however, predicts a much higher temperature [18]. This leads us to conclude that either the classical treatment of the atomic motion used in deducing T is invalid, or that other factors, such as heating effects of the interacting beam or imperfections in the focusing lenses used on the beam, also contributed in reducing extinction. In Chapter 4 we propose a sub-recoil cooling scheme to cool the atom to its vibrational ground state and describe the experimental setup constructed for this purpose. Preliminary measurements on the coherence time of the relevant transition to determine the viability of such a scheme shows that the coherence time is an order of magnitude less than the necessary. An alternative is suggested.

Chapter 2

Trapping and interrogating a single atom

In this chapter we present the single ^{87}Rb atom trap and the methods used in Tey's experiment in which the extinction of a weak coherent beam by the atom was measured [1].

2.1 Experimental Setup

Figure 2.1 illustrates the experimental setup. We trap a single ^{87}Rb atom in a tightly-focused, far-off-resonant dipole trap (FORT, $\lambda = 980\text{ nm}$) at the focus between a pair of aspheric lenses (LightPath Technologies Inc. no. 350230, full NA= 0.55, $f = 4.5\text{ mm}$). Cold atoms are loaded into the FORT from a magneto-optical trap (MOT) surrounding the FORT ¹. A MOT is required as a source of cold atoms because it has the velocity capture range

¹Full specifications of the MOT can be found in [2].

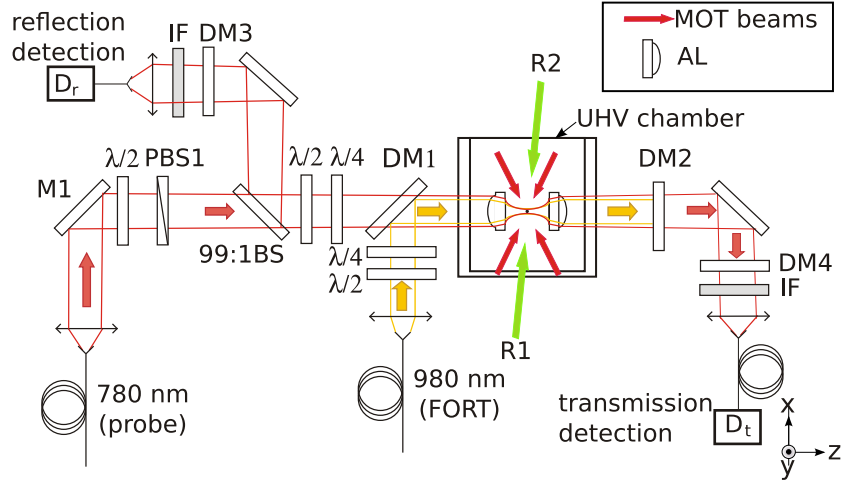


Figure 2.1: Experimental setup for measuring the extinction of a light beam by a single ^{87}Rb atom. AL: aspheric lens ($f = 4.5$ mm, full NA = 0.55, AR-coated for near-IR wavelengths). UHV: ultra-high vacuum chamber (10^{-10} Torr). DM: dichroic mirror. BS: beam splitter with 99% reflectivity. $\lambda/4$: quarterwave plate (QWP). $\lambda/2$: halfwave (HWP) plate. HWPs and QWPs convert the linearly polarised FORT and probe light into circularly-polarized light. IF: interference filter centered at 780 nm, D_r and D_t : Si-avalanche photodiodes. R1 and R2: Raman beams (details see fig 4.3). Not shown: a) Two more horizontal MOT beams lie in an orthogonal plane (see Fig. 2.2). b) MOT quadrupole magnetic field anti-Helmholtz coils. c) Biased magnetic field creating Helmholtz coils zero the magnetic field at trap centre. d) Tilted DM2 prevents FORT back-reflection into UHV.

required to trap ^{87}Rb atoms initially at room temperature [16]. The ^{87}Rb source is from a dispenser wire within the UHV chamber which releases the atoms when a DC current is passed through it.

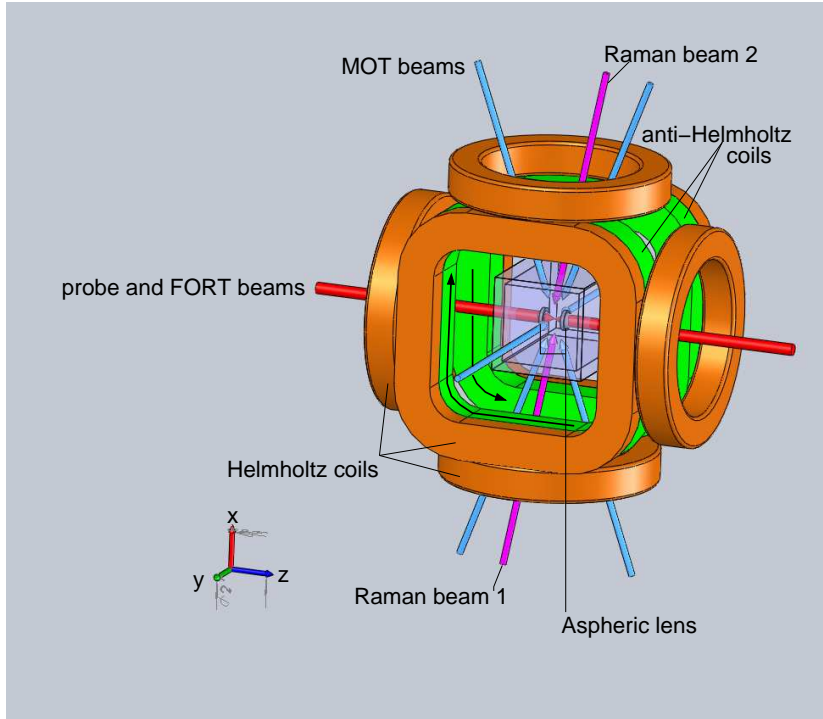


Figure 2.2: The core of the setup including a magneto-optical trap, a cuvette attached to a vacuum (UHV) chamber, the aspheric lenses, and the relevant light beams used for trapping the atom and performing the extinction experiment (the lens holder in the cuvette is not shown for clarity). Raman beams drive the transition between the two hyperfine-ground states are performed in a separate experiment (see Chapter 4). Black arrows indicate anti-Helmholtz coil current direction. Polarisation (left-hand circularly polarised/LHC or right-hand circularly polarised/RHC) of MOT beams are LHC for beams lying in the XZ-plane, but RHC for beams along the Y axis. Picture not drawn to scale.

2.1.1 Magneto Optical Trap

The magneto-optical trap consists of three pair of counter-propagating beams that intersect in a small volume at the FORT focus within the UHV chamber and subjected to a quadrupole magnetic field gradient. It captures and cools atoms, confining them such that the FORT loads effectively². We describe

²A full description of the operating principles of a MOT and Doppler cooling is beyond the scope of this work and the reader is directed to [19, 16].

the components:

1. Two monochromatic lasers (**MOT beams**): a) Cooling beam ($\tilde{780}$ nm): red-detuned about 4 linewidths (1 linewidth = $2\pi \cdot 6$ MHz) from the cooling transition $|5S_{1/2}, F = 2\rangle \rightarrow |5P_{3/2}, F' = 3\rangle$ b) Repump beam ($\tilde{795}$ nm): on-resonance to a repump transition $|5S_{1/2}, F = 1\rangle \rightarrow |5P_{1/2}, F' = 2\rangle$ (see Grotrian diagram in fig A.1). The repump laser pumps the atom out from the $|5S_{1/2}, F = 1\rangle$ hyperfine state, such that spontaneous decay from $|5P_{1/2}, F' = 2\rangle$ allows the atom to return to state $|5S_{1/2}, F = 2\rangle$ – an atom in $|5S_{1/2}, F = 1\rangle$ is unable to interact with the cooling beam. The cooling and repump beams are delivered together as three counter-propagating beam pairs that perform ‘optical molasses cooling’.³ The combined power of all six beams are: $P_{cool} = 900 \mu\text{W}$, $P_{repump} = 100 \mu\text{W}$ with an estimated beam waist of 1 mm at the trap centre.

The MOT beam polarisations⁴ are adjusted to that described in Figure 2.2 (caption), consistent with the orientation of the quadrupole field gradient dictated by the direction of the anti-Helmholtz coil currents. [16]

³Optical molasses: By red-detuning the MOT beams with respect to the atomic resonance, an atom becomes more on-resonant with the laser beam opposing its velocity than the one propagating along its velocity, due to the Doppler effect. By interacting more strongly with the opposing beam, the atom loses momentum during the absorption process. The atom now in an excited state, spontaneously emits a photon and recoils in a random direction. Over many absorption-emission cycles, the velocity along the beam axis is reduced by the absorption process, while the time-averaged gain in velocity during the random recoil vanishes. This results in cooling. For small enough velocities, the slowing force is proportional to its velocity [19], resulting in viscous damping, giving rise to its name ‘optical molasses’.

⁴Polarisation convention: In this work, the polarisation of a beam is said to be RHC if the polarisation vector rotates clockwise when facing into the oncoming wave.

2. Quadrupole magnetic field created by two anti-Helmholtz coils (**MOT coils**) create magnetic field gradients at 7 Gauss cm⁻¹ along \hat{y} and 3.5 Gauss cm⁻¹ along \hat{x} and \hat{z} at the trap centre (see coordinate system in fig 2.2).

It is noteworthy that without the the quadrupole field, the MOT beams form optical molasses: On their own, each counter-propagating pair perform Doppler cooling – the quadrupole field enhances the Doppler cooling mechanism such that it is more effective at positions further away from the trap centre. The position-dependent cooling force compresses the atoms towards the centre [19], forming a trapped cloud of cold atoms.

3. Bias magnetic fields along all axes created by three pairs of Helmholtz coils cancel ambient magnetic fields (assumed time-independent) at the trap centre such that the zero field position coincides with the FORT focus, the intersection point for all three MOT beams and the centre of the quadrupole field – creating a MOT positionally stable around the FORT focus.

2.1.2 Far off-resonant dipole trap (FORT)

At the focus, the FORT beam waist is 1.56 μm and has a power of 21 mW resulting in a maximal trapping potential $U_0 = k_B \cdot 1.3 \text{ mK} = h \cdot 27 \text{ MHz}$. For an atom localised about the vicinity of the focus, the FORT potential can be approximated to be harmonic, characterised by transverse (ω_x, ω_y) and longitudinal (ω_z) trap frequencies (see Section A.2.2). The collisional-

blockade mechanism [20] in the micron-sized FORT allows only one atom in the trap.⁵

For a cylindrically-symmetric FORT formed by a beam with a Gaussian intensity profile, the transverse trap frequencies are estimated to be $\omega_x = \omega_y = 2\pi \cdot 80$ kHz, while the longitudinal trap frequency is at $\omega_z = 2\pi \cdot 13$ kHz. We relegate the calculation of these parameters to Section A.2.

When the atom is trapped in the FORT, MOT beams (780 nm and 795 nm) scattered by the atom at focus of the aspheric lenses, causes photon counts detected at D_r to spike. This serves as a signal which we use to initiate the extinction experiment. When illuminated by the MOT beams, the presence of a single atom can be confirmed by observing strong photon anti-bunching on the second-order correlation function for the photons [1] scattered in opposite directions into detectors D_t and D_r .

The polarisation of the FORT light was chosen to complement the extinction experiment: Figure 2.3 shows the calculated AC Stark shift [1] of the $5S_{1/2}, F = 2$ and $5P_{3/2}, F' = 3$ hyperfine states of ^{87}Rb perturbed by a left-hand circularly (LHC) polarised FORT. The LHC FORT produces a non-degenerate Zeeman sublevel splitting not possible with a linear FORT (see Section A.2). This allows us to isolate $|g+\rangle(|g-\rangle)$ and $|e+\rangle(|e-\rangle)$ from the other m_F states (see fig 2.3). This is beneficial as one would expect to observe maximum extinction for a clean two-level system, with no other decay channels. A bias magnetic field of about 2 Gauss along \hat{z} generated by

⁵Collisional blockade: The inelastic collisional loss coefficient of a FORT is inversely proportional to its trap volume [20]. At a small enough waists, the loss coefficient is so large that the FORT cannot retain more than one atom at a time. Light-assisted inelastic collisions mediated by the MOT beams convert internal atomic energies to kinetic energies shared by the colliding bodies, thus repeling both atoms out of the trap.[21]

To prevent Larmor precession of the atom caused by magnetic fields orthogonal to the quantisation axis (e.g. earth’s magnetic field at 0.3-0.6 Gauss), we carefully zero the magnetic field at the centre of the trap to an uncertainty of ± 10 mGauss along the three coordinate axes, by applying magnetic field biases with the Helmholtz coils. Larmor precession is undesirable as it causes the population to leak from $|g_{\pm}\rangle$ or $|e_{\pm}\rangle$ to other $|m_F\rangle$ and $|m_{F'}\rangle$ states, preventing the probing of an ideal two-level system.

2.2 Extinction Experimental Sequence

The extinction experiment is carried out in several steps on the single atom, and repeated for several similarly trapped atoms. Figure 2.4 illustrates the temporal sequence of the experiment.

1. When an atom is in the FORT we detect a signal of ~ 4200 photons s^{-1} at D_r as compared to a background count rate of $600 s^{-1}$ for an empty trap; the background count is due mainly to scattered MOT beams by the MOT cloud in the vicinity of the lens focus. Using a pattern-generator to integrate photon counts detected at D_r due to the atom scattering MOT beam photons, we may determine a threshold photon count for which we are certain the atom is loaded in the FORT within 20 ms of the loading event ⁶. Crossing this threshold triggers the following steps.

⁶Given the signal-to-noise ratio we require 10 to 30 ms to reliably determine the presence of the atom [2].

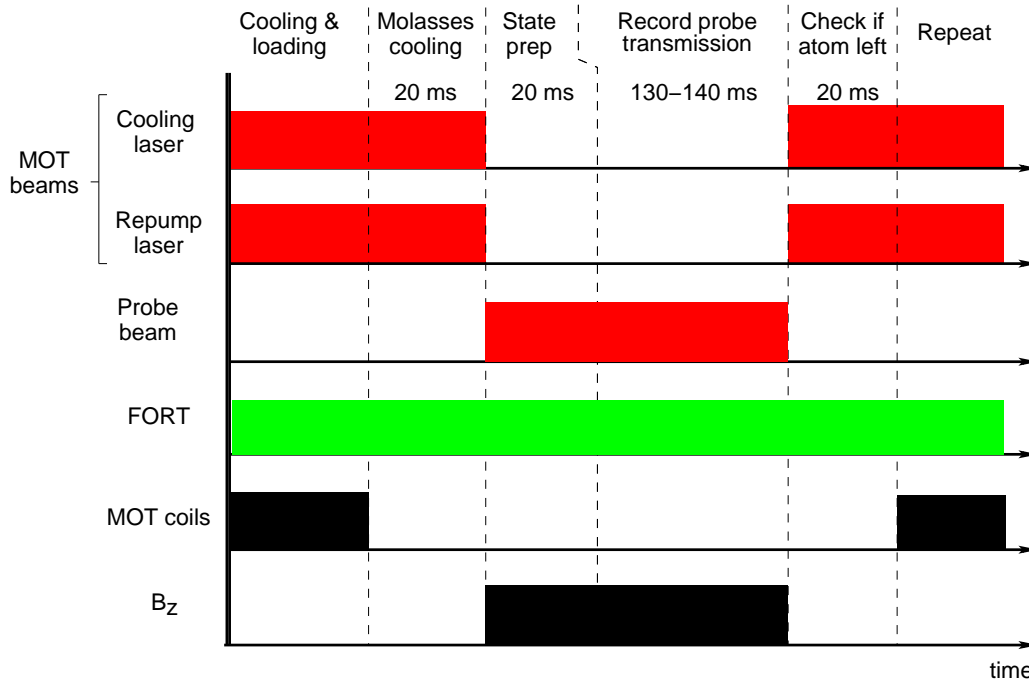


Figure 2.4: Schematic of the temporal sequence for the experiment measuring the extinction of a probe beam by a single atom. The repump beam operating together with the probe beam (see Section 2.2 step 3) is not illustrated. Details in text.

2. Once the atom loads, we extinguish the MOT cloud by turning off the quadrupole magnetic field. This prevents the loading of another atom in the FORT; the presence of more than one atom causes both atoms to be ejected, due to the collisional-blockade mechanism. Additional kinetic energy is removed by the MOT beams which remain for another 20 ms, performing optical molasses cooling. This is required as the FORT is a conservative potential; the atom will leave the trap unless the additional kinetic energy gained by entering a negative potential trap is removed. The typical trap lifetime for this procedure is 1 s. At the same time, a magnetic field bias of ~ 2 Gauss along \hat{z} is turned on;

the same 20 ms allows the Helmholtz coil currents supplying this field to stabilise.

3. After molasses cooling, we use a LHC(RHC) probe beam (see fig 2.3) to optically excite σ^+ (σ^-) transitions $|5S_{1/2}, F = 2, m_F\rangle \rightarrow |5P_{3/2}, F' = 3, m_F + (-)1\rangle$, pumping the atom into $|g+\rangle$ ($|g-\rangle$). This state preparation step takes 20 ms. A repump beam that is resonant to the transition $|5S_{1/2}, F = 1\rangle$ to $|5P_{1/2}, F' = 2\rangle$ prevents the atom from being pumped into the $(5S_{1/2}, F = 1)$ manifold, which does not couple to the probe beam. The repump beam is always turned on together with the probe beam for the extinction experimental sequence.

Before the sequence, the probe photon scattering rate at the atom was fixed at $R_{probe} = 2500 \text{ s}^{-1}$, such that the net recoil energy $R_{probe} \cdot E_{recoil} \cdot 2\pi/\omega_{x(z)}$ gained per oscillation period $\tau_{x(z)} = 2\pi/\omega_{x(z)}$ is much smaller than one vibrational quanta of energy $\hbar \cdot \omega_{x(z)}$ of the trapping potential. This prevents the beams from heating the atom out from the FORT. For an atom decaying from $|e+\rangle$ ($|e-\rangle$), the recoil energy of the atom is $E_{recoil} \approx h \cdot 6.8 \text{ kHz}$.

4. Since there is a finite chance that the atom leaves the FORT any time within the typical lifetime ($\sim 1 \text{ s}$) that the atom remains in the trap, there is a need to intermittently measure transmitted probe photon counts at D_t , and check if the atom remained in the trap thereafter, at regular intervals. Otherwise, if we measure photon counts for the whole duration of $\sim 1 \text{ s}$ when in actuality the atom is in the trap for only a fraction of the time, we measure the time-averaged value for the

transmission instead of its instantaneous value. We record the transmitted photon count n_i^{atom} with the atom in the FORT by integrating photon counts at detector D_t for the i -th time interval t_i^{atom} , ranging from 130–140 ms. Without switching off the probe beam, the MOT beams are turned on for about 20 ms, probing for atomic fluorescence above background count rates. This indicates if the atom still remains in the trap after the short interaction time with the probe. The photon counts at D_t are not recorded when the atom is illuminated by the MOT beams. If the atom is determined to be still in the trap, steps 3 and 4 are repeated. Otherwise, we record the transmitted probe photon count n^{noatom} without the atom with detector D_t for $t^{noatom} = 2 s$.

For a series of contiguous measurement intervals of the same atom, we calculate a transmission value T by

$$T = \frac{\sum_i n_i^{atom} / t_i^{atom}}{n^{noatom} / t^{noatom}} \quad (2.1)$$

where the subscript i refers to the i -th time interval.

5. We turn on the MOT beams and quadrupole coil again, and wait for another atom to be trapped in the FORT, triggering step 2.

For a hundred similarly trapped atoms, we obtain a mean transmission value \bar{T} , each trapping event weighted by w :

$$\frac{1}{w} = \frac{1}{\sum_i t_i^{atom}} + \frac{1}{t^{noatom}} \quad (2.2)$$

This is because the time which an atom remains in the FORT varies between different trapping events, and so T has a different uncertainty for each event [2]. Note that the index i runs over a set of contiguous measurement events belonging to the same trapping event. This weighing factor was chosen as it minimises the error of \bar{T} for a fixed number of trapping events. The average extinction value of the probe is therefore $1 - \bar{T}$.

2.3 Conclusions of Extinction Experiment

For a tightly-focused, weakly coherent probe at a waist $0.8 \mu\text{m}$ at the atom (corresponding to incident probe beam waist of 1.4 mm at the aspheric lens), a substantial extinction ratio of up to $10.4 (0.1)\%$ by the single ^{87}Rb atom was obtained by Tey et al. [1]. However, by computing the electric field strength of the probe at the FORT focus, it was calculated that an atom at rest in the trap should have a maximum extinction well over 20% (see fig 3.4.1, blue curve at beam waist= 1.4 mm).

There are a few possible explanations:

1. The electric field strength of the probe was calculated assuming that the aspheric lenses used in its focusing were ideal – real lenses introduce spherical aberrations to a focused field, decreasing the field amplitude and thereby the measured extinction.
2. Since the probe is focused to a diffraction limited spot – a size of the same order as the atomic scattering cross section, inadequate localisation of the atom in the FORT causes the atom to experience lower

field amplitudes as it ventures away from the probe focus. Characterising the energy distribution of an ensemble of single trapped atoms in the FORT by a Maxwell-Boltzmann temperature, the dependence of extinction with temperature was obtained by Teo. C [18]. In Chapter 3 we determine experimentally this temperature in order to compare with the model in [18]. Hence we deduce that the motion of the atom is not the only reason why the extinction decreased by 50% from its theoretical value.

Chapter 3

Energy distribution of a single atom in the FORT

In this chapter, we present an experiment which quantifies the energy distribution of an ensemble¹ of trapped ^{87}Rb atoms in a FORT. The procedure follows C. Tuchendler et al. [3] where the energy distribution was determined by the probability of recapturing the atom after releasing it from its trapping potential for a variable amount of time. Assuming a Maxwell-Boltzmann model for the measured energy distribution, the ensemble temperature² was extracted. The temperature is compared with a calculation on the temperature dependence of the extinction of the probe beam by the single atom, to determine if temperature effects account mainly for the reduction in extinction.

¹By an ensemble, we refer to the set of similarly trapped single atom events.

²Normally, it does not make sense to talk about the temperature of a single atom. The ensemble temperature however, refers to the temperature parameter T which characterises the Maxwell-Boltzmann energy distribution of a set single atom trapping events.

While time-of-flight imaging has been used to extract temperature and spatial density information of ultra-cold atomic gases [23], imaging techniques for single atoms have only been developed recently [24] shortly after near-unity efficiency imaging methods at ultra-high spatial resolutions of close to $10\ \mu\text{m}$ have been used to detect the presence of a single atom [25]. The release and recapture technique was preferred over these methods as it is much simpler to implement with the existing setup.

3.1 Release-recapture experimental sequence

The idea behind this method of determining the temperature is that by switching off the dipole trap for a period Δt , the probability of recapturing the atom $P_{RR}(\Delta t)$ after restarting the trap depends on its initial energy. By temperature we mean the parameter which characterises the energy distribution of a statistical ensemble of single atoms which we repetitively trap. This method is particularly robust against noise sources, such as fluctuations in fluorescence intensity of the atom used to detect the atom's presence in the trap because the measurement outcome is binary: either we detect the background fluorescence intensity, or a much higher fluorescence intensity produced by a single scatterer in the trap [3].

Figure 3.1 illustrates the experimental sequence: The MOT beams and coils are initially turned on, creating the MOT cloud of atoms which loads the FORT. Once loading is detected, the atom is pumped into the closed cyclic transition $|5S_{1/2}, F = 2, m_F = 2\rangle \leftrightarrow |5P_{3/2}, F' = 3, m'_F = 3\rangle$ with a σ^+ probe beam with the help of a repump beam driving the $|5S_{1/2}, F = 1\rangle \rightarrow$

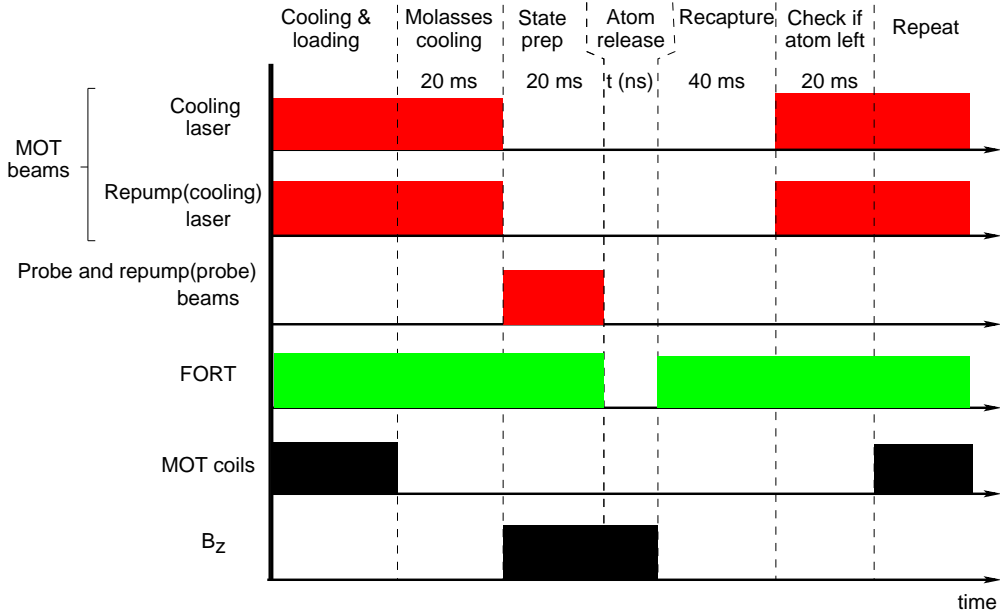


Figure 3.1: Schematic of the temporal sequence for Release and recapture experiment. Details in text.

$|5P_{1/2}, F' = 2\rangle$ transition for 20 ms. A static magnetic field ~ 2 Gauss along \hat{z} is turned on to augment the Zeeman sublevel splitting in the $(5S_{1/2}, F = 2)$ manifold. The aforementioned stages emulates the conditions of the atom **just before** it was probed in the extinction experiment – the temperature at this stage of the extinction experiment is the quantity of interest.

The FORT was turned off within $t_{off} = 70(10)$ ns by an acousto-optical modulator (AOM) for time Δt . To recapture the atom, we restarted the trap suddenly, within $t_{on} = 70(10)$ ns, and wait for 40 ms³ before checking

³The 40 ms wait was introduced because at this stage, we also turn off the Helmholtz coil supplying the $B_z = \sim 2$ Gauss static magnetic field. Due to eddy-currents, the current in the coils required time to dissipate. Switching off the bias field reduced the Zeeman sublevel splitting back to its original value, from ~ 1 MHz to 300 kHz between adjacent m_F levels in the $|5S_{1/2}, F = 2\rangle$ manifold. Though we did not verify, the reduced non-degeneracy was presumed to allow this manifold to couple more strongly with the MOT cooling beam (see fig A.1, cooling beam), whose transition linewidth is about 6 MHz.

the atom for scattered photons by illuminating it with the MOT beams.

The shut-off (t_{off}) and turn-on (t_{on}) time of the FORT light was determined in a separate experiment by determining the fall and rise times of the FORT light intensity using a fast photodiode (Hamamatsu S5973). Measuring this time we determined that the trap could be turned on and off almost instantaneously compared to the trap oscillation period $2\pi/\omega_\rho, 2\pi/\omega_z$ (tens of μs). Otherwise, we would have to model the dynamics of the atom as it oscillates in a trap with a slowly varying depth, which makes the simulation (see Section 3.2) of the release and recapture experiment, necessary to process the experimental data, more complicated.

To see why a fast shut-off time is important we can think of the atom in the 3D harmonic FORT potential as an oscillating mass acted on by a spring. To simplify the analogy let us consider the motion only in one dimension in a horizontal line without considering gravity. When the trap is turned off instantaneously, it is equivalent to thinking about the spring being immediately ‘hooked off’ from the mass, and the spring no longer causes the mass to accelerate. We thus take a ‘snapshot’ of the mass’s instantaneous position and velocity which remains the same after the spring is removed, unless of course acted upon by another force. However, if the FORT light switches off within a time scale on the order of the trap frequency, this is equivalent to a time varying spring constant in the spring–mass analogy, before the spring is completely unhooked. We thus have to determine the final velocity of the mass under these dynamics, which can be challenging to model in a simulation if the time-dependence of the spring constant does not have a closed-analytic expression.

After recording whether the atom remained in the FORT, the experimental sequence is repeated for an ensemble of atoms, determining the probability $P_{RR}(\Delta t)$ that the atom remains in the trap after variable release time Δt .

3.2 Extracting the temperature

In order to connect measured data of the recapture probability with the temperature of the atomic ensemble in the experiment, we perform a Monte-Carlo simulation on the trajectory of the single atoms assuming a Maxwell-Boltzmann distribution of initial energies⁴ in the trap to determine the probability of recapturing it after it is released for Δt .

Approximating the trapping potential as a 3D harmonic potential, we randomly generate⁵ the initial position-momentum vector $(x_i, y_i, z_i, v_{x,i}, v_{y,i}, v_{z,i})$ of the atom based on a randomly generated value for its total energy, obtained from a probability distribution obeying the Maxwell-Boltzmann, at temperature T . After free fall for Δt , this vector becomes $(x_i + v_{x,i}\Delta t - g\Delta t^2, y_i + v_{y,i}\Delta t, z_i + v_{z,i}\Delta t, v_{x,i}, v_{y,i} + g\Delta t, v_{z,i}) = (\vec{r}_f, \vec{v}_f)$.

Because the trap restarts at a time scale (70 ns) much faster than the trap oscillation periods ($\tau_\rho = 12.5 \mu\text{s}$, $\tau_z = 76.9 \mu\text{s}$), the atom will accelerate under the FORT potential with an initial velocity \vec{v}_f at position \vec{r}_f ; the same values as it were in free space. For a conservative harmonic potential, the total energy of the atom is a conserved quantity. Thus by calculating

⁴The energy distribution of a statistical ensemble of single atoms in a microscopic trap subjected to Doppler cooling was verified to be Maxwell-Boltzmann [3].

⁵By means of the Metropolis-Hastings algorithm, taking into account the position-momentum probability distribution in a classical harmonic oscillator.

the initial energy of the atom in the FORT at \vec{r}_f , we know its total energy everywhere in the trap – if the atom did not have enough energy to escape the FORT potential at \vec{r}_f , it will never escape it in its subsequent motion. In reality though, the atom-FORT system is not a closed system because the ever present ^{87}Rb vapour within the cuvette used to load the MOT threatens to kick the atom out from the trap.

The total energy $E(\vec{r}_f, \vec{v}_f) = T(\vec{v}_f) + U(\vec{r}_f)$ is computed, where $U(\vec{r}_f)$ is the trap potential at \vec{r}_f . Recalling that the trap potential is negative, we know that the atom remains trapped in the FORT only when $E(\vec{r}_f, \vec{v}_f) \leq 0$, and escapes otherwise. In the simulation, the trap potential along \hat{x} parallel to the earth’s gravitational field was not moderated by the atom’s gravitational potential energy as the modifications were calculated to be 4 orders of magnitude smaller than the trap potential. By simulating 500,000 such trajectories, the probability of recapture as a function of release time was generated.

In the experiment, we measured at zero release time: $P_{RR}(\Delta t = 0) = 0.82$, possibly due to non-negligible loss mechanisms, such as the background ^{87}Rb vapour pressure in the UHV and probe beam scattering effects. Assuming that the probability of losing the atom due to these effects is relatively constant for the range of release times (μs) varied in the experiment⁶, we may scale all points of the Monte-Carlo simulation by $P_{RR}(\Delta t = 0)$, to better fit to the experimental data. Figure 3.2 shows the typical results generated by the capture-release experiment (dots) with the ones by the Monte-Carlo

⁶A valid assumption because an atom remains trapped for a much longer time scale between 200 ms–1 s compared to all possible Δt used in the release-recapture experiment.

simulation (line).

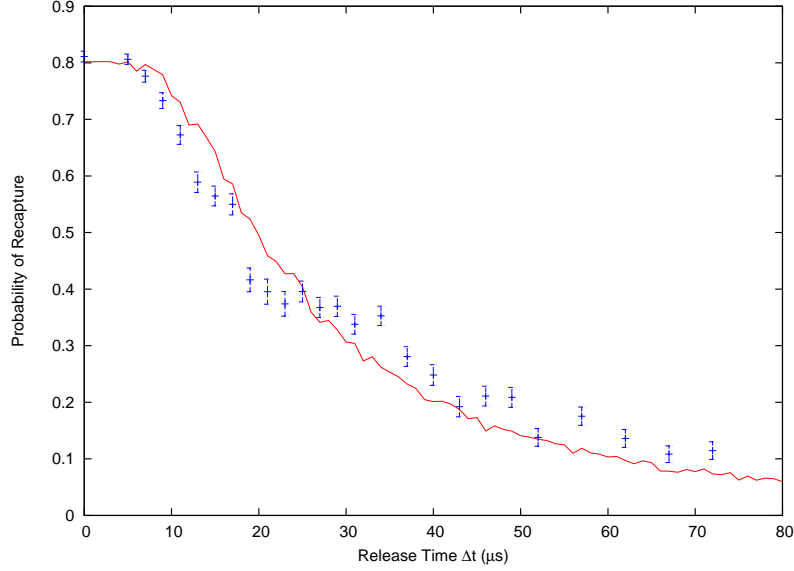


Figure 3.2: (Blue dots) Experimental results showing the probability of recapturing the atom $P_{RR}(\Delta t)$ as a function of release time Δt with error bars (statistical, assuming a binomial distribution of each recapture event). Each data point is the accumulation of at least 100 sequences. (Red curve) Fit by the Monte Carlo simulation of the release and recapture method, which is the average of 500,000 trajectories for each release time, at best-fit temperature $T = 34.6(5) \mu\text{K}$. Fit parameters: FORT trap depth 1.3 mK, FORT waist 1.56 μm .

The simulation is repeated for a range of temperatures. The best fit temperature is the one which minimises the χ^2 value between the experimental data and simulated results for each temperature where $\chi^2 = \sum_j (f_j - P_{RR}(\Delta t_j))^2 / \sigma_j^2$. Here, σ_j is the standard-error of the j -th experimental point (corresponding to release time Δt_j) and f_j is the simulated point.

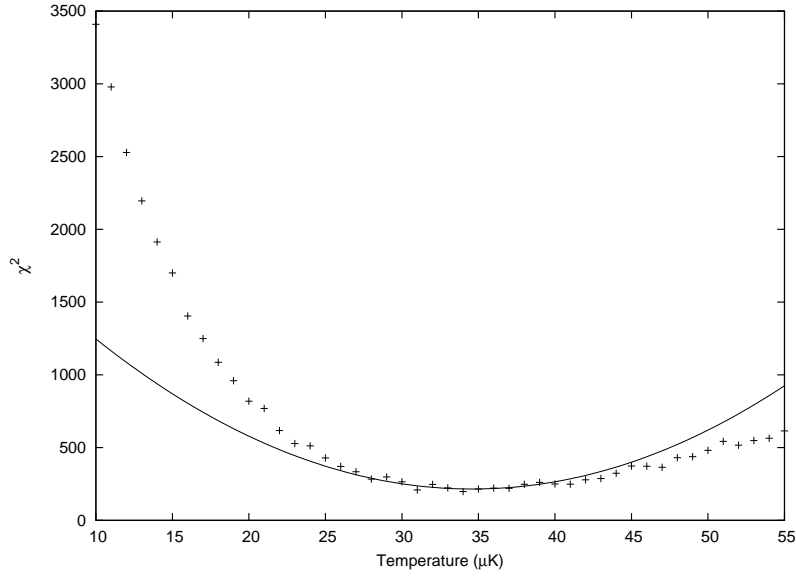


Figure 3.3: Plot of χ^2 for different values of T used in the Monte-Carlo simulation (crosses). Fitting for $T = 30$ to $40 \mu\text{K}$ to a parabolic function (solid curve) yields $\chi^2 = a * (T - T_o)^2 + c$ with $a = 1.7(6) \mu\text{K}^{-2}$, $T_o = 34.6(5) \mu\text{K}$, $c = 215(8)$. Errors in brackets reflect the error in fitting to a parabolic function.

3.3 Results

Figure 3.3 illustrates χ^2 as a function of various temperatures. Due to the large event sample, we may assume that the χ^2 function varies parabolically in the vicinity of the temperature that minimizes χ^2 [26]. Further, we compute the variation [26] of T

$$\sigma_T^2 = 2 \left(\frac{\partial^2 \chi^2}{\partial T^2} \right)^{-1}$$

where $\frac{\partial^2 \chi^2}{\partial T^2}$ can be obtained from the fit parameter a (see figure 3.3). This yields a standard deviation of $\sigma_T = 1 \mu\text{K}$.

The best fit temperature $35(1) \mu\text{K}$ is well below the Doppler cooling limit

temperature $144\ \mu\text{K}$ (when $F = 2$ to $F' = 3$ is used for the cooling transition). The ratio between the trap depth and the temperature is 37, indicating that we are in the harmonic regime of the trapping potential.

3.4 Discussion

3.4.1 Comparison with Probe extinction

The expected values for the probe extinction was recently calculated as a function of ensemble temperature [18]. Treating the atom as a classical particle, an atom oscillating in the FORT will observe a position-dependent AC Stark shift in its probe transition resonance frequency, causing it to be out of resonance to the probe beam. This is because the AC Stark shift is directly proportional to the FORT field intensity (see Section A.2.1), which has a Gaussian distribution. Higher temperatures thus imply higher oscillation amplitudes, and the time-averaged absorption of the probe decreases as the atom ventures away from the optimal position where the AC Stark shifted resonance of the probe transition is on-resonance with the probe frequency. The result of calculating the extinction dependence on ensemble temperature is illustrated in Figure 3.4 by the solid curves.

Comparing the experimental extinction (fig 3.4.1, red crosses) with the calculated values for the extinction at $T = 10\ \mu\text{K}$ (solid red curve) and $T = 150\ \mu\text{K}$ (green solid curve), we would expect the experimental extinction for $T \sim 35\ \mu\text{K}$, to lie somewhere between the red and green curves, but they do not.

Extinction vs beam waist (Full 3d)

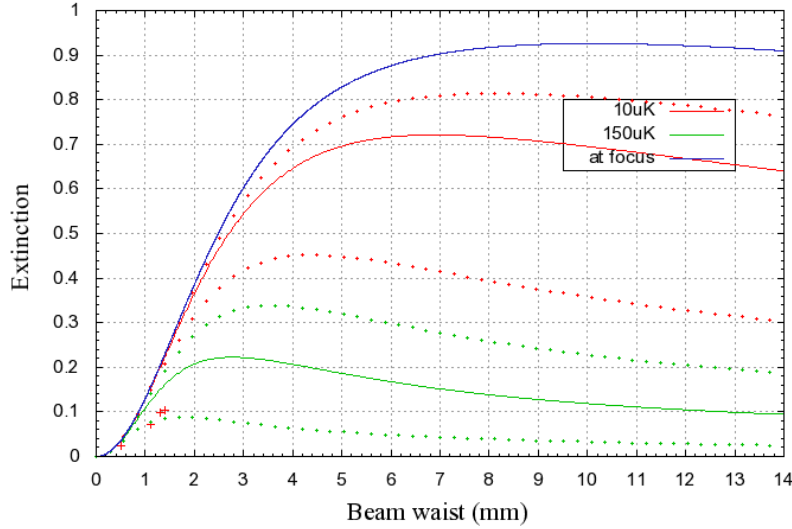


Figure 3.4: Solid curves: Dependence of probe extinction on beam waist incident on the aspheric lens, calculated for different atom temperatures [18]. Larger incident waists result in stronger focusing. FORT parameters used in the calculation are: trap frequencies $\omega_\rho = 80$ kHz and $\omega_z = 13$ kHz. Dotted curves: limits of dependence curves calculated at trap frequencies $\pm 50\%$ from predicted values. Red crosses: Measured probe extinction.

As the trap frequencies were computed (see Section A.2.2) assuming a paraxial approximation for the probe beam, Teo. C repeated the above calculation for errors ($\pm 50\%$) in the trap frequencies (dotted lines), which places T near $150 \mu\text{K}$. On hindsight, an independent experiment which involves the parametric heating of atom in the FORT [27] could have been performed to measure the actual trap frequencies. Assuming though, that the trap frequencies are correctly computed, we can only conclude that for $T \sim 35 \mu\text{K}$, the measured extinction values are much lower than expected, and so other effects, such as using a non-ideal lens in propagating the probe field, are non-negligible in explaining the reduction of extinction.

3.4.2 Validity of classical treatment

The trajectory simulation for the capture and release experiment assumes that the atomic motion could be described classically, which becomes invalid when mean vibrational quantum numbers are small. The probe extinction calculation in Section 3.4.1 also assumes classical trajectories.

Evaluating the mean vibrational quanta in Section A.3 for $T = 35 \mu\text{K}$, we have $\bar{n}_x = \bar{n}_y = \bar{n}_\rho = 8.6$ and $\bar{n}_z = 55.6$. A full quantum treatment of the simulation is beyond the scope of this project, but an alternate proposal to experimentally determine $\bar{n}_{\rho,z}$ by means of resolving individual vibrational levels is suggested in Section 4.5.

The following questions are posted to the reader, and may deserve further investigation:

1. During the release procedure, does a significant portion of the atomic wavefunction spread back into the trap? This may account for higher recapture probabilities leading to a lower temperature measurement.
2. Is it possible that for odd vibrational Fock states, we see smaller extinction of the probe due to a vanishing probability density function at the trap centre, where the probe electric field is the highest?
3. Is there significant impulse imparted to the atom when the trap restarts in the release and recapture experiment?

Chapter 4

Towards resolved-sideband

Raman Cooling

4.1 Background

The atom experiences a negative harmonic potential which is deepest where the FORT intensity is maximum (see Section A.2.1). As the wavelength of the FORT is far detuned from any possible transition from the ground state of ^{87}Rb , the atom does not scatter a significant number of FORT photons and its total energy remains the same; the potential is conservative. In the extinction experiment [1], the FORT is always switched on. As an atom loads the magneto-optical trap localised around the FORT from free space, its potential energy decreases while its kinetic energy increases but its total energy remains positive and unchanged and would never be bounded by the FORT.

Removing the kinetic energy to the point where the total energy of the

atom is below zero is achieved in our setup by Doppler cooling with the MOT beams (see Section 2.2). After cooling, the probability density function of the atom's total energy can be characterised by the Maxwell-Boltzmann distribution at $T = 35(1) \mu\text{K}$, lower than the theoretical limit imposed by the Doppler cooling limit ($T_{dopp} = 144 \mu\text{K}$). This leads us to conclude that a sub-Doppler cooling mechanism is active during this cooling stage.

4.1.1 Sub-Doppler cooling in the FORT

A complete description of sub-Doppler cooling is beyond the scope of this work, but we give a qualitative explanation [28]. For simplicity of explanation, we consider only one pair of counter-propagating cooling beams driving the $(5S_{1/2}, F = 2)$ to $(5P_{3/2}, F' = 3)$ transition, cooling an atom in free space moving along the beam axis.

1. In the experiment, the polarisation of the MOT beams is such that for each counter-propagating beam pair, one drives the σ^+ transition, the other drives the σ^- transition. This corresponds to each beam being left-hand circularly polarised. The resultant polarisation for the combined field is linear everywhere but rotates along the beam axis with a pitch of $\lambda_{cool}/2$, where λ_{cool} is the cooling beam wavelength at 780 nm.
2. For a stationary atom, the linearly polarised MOT field induces differential AC Stark shifts in the Zeeman sublevel structure of $(5S_{1/2}, F = 2)$, the $m_F = 0$ state is energy shifted lower than any other magnetic sublevel [28].

3. At the same time, as a consequence of the branching ratios governing the spontaneous emissions from $(5P_{3/2}, F' = 3)$ to the different Zeeman levels in the ground state, it can be shown that the linearly polarised MOT field optically pumps the atom into the $(5S_{1/2}, F = 2, m_F = 0)$ sublevel [28]. The time scale of this optical pumping depends on the MOT beam intensity, but is typically several natural lifetimes of the $(5P_{3/2}, F' = 3)$ state.
4. Suppose the atom starts moving towards the σ^+ beam, this red-detuned σ^+ beam is Doppler shifted nearer to resonance and so the atom couples more strongly to this beam, rather than the σ^- beam, and becomes optically pumped towards the positive m_F levels. As the transition probability for the σ^+ transitions are larger than the σ^- transitions for positive m_F states [29], optical pumping towards the positive m_F is further enhanced, helping to scatter even more σ^+ light.

If the atom is in the FORT, the atomic levels undergo further AC Stark shifts, causing them to shift either further or closer to resonance with the cooling beams. This moderates the scattering rate of the σ^+ beam, which may result in a lower cooling force.

5. In summary, redistribution of the population by the σ^+ beam helps enhance its scattering rate compared to the σ^- beam, imposing a larger cooling force on the atom than what one anticipates from the Doppler cooling mechanism alone. This results in a temperature lower than the Doppler temperature $T_{dopp} = 144 \mu\text{K}$.

As the scattering of cooling beam photons is required for cooling, the lowest temperature achievable is limited by the recoil energy of the atom. A sub-recoil cooling technique would require the atom to be decoupled from the cooling beam once it reaches the desired temperature, such that it ceases to recoil from the scattering of photons. The technique must also be very energy selective, so that the variance of temperatures around the desired value is minimised.

4.1.2 Sub-Recoil cooling in the FORT

In this section we introduce conceptually how to perform sub-recoil cooling by driving a two-photon Raman transition between two hyperfine ground states. A detailed treatment is given in Section A.4.

Consider a three level atom with hyperfine ground states $|\uparrow\rangle$ and $|\downarrow\rangle$ frequency separated by ω_0 (see figure 4.1) with internal states dressed by the vibrational Fock states, due to its motion in the x-axis¹. The atom is illuminated by two Raman beams at frequencies ω_α and ω_β respectively. The two beams counter-propagate along the x-axis. As a pedagogical example, consider an atom originally in state $|\uparrow, n_x = 2\rangle$ driven by a two-photon Raman transition π -pulse into the $|\downarrow, n_x = 1\rangle$ state. The resonance condition for this transition requires the two-photon detuning to be $\omega_\beta - \omega_\alpha = \omega_0 + \delta_\omega = \omega_0 + \omega_x - \Delta$, where Δ is small compared to the linewidth of the transition. The transition is realised only for small Δ provided we set the duration of the π -pulse to be much longer than the inverse of the trap frequency ($2\pi/\omega_x$)

¹We consider motion in one dimension for simplicity.

cooled atom to gain vibrational quanta ($\Delta n_x = 0$) is low only when the vibrational energy quantum ($\hbar\omega_x$) is much larger than the atomic recoil energy ($\hbar^2\omega_{pump}^2/(2m)$) where m is the atom's mass.

Thus we see how a two-photon Raman π -transition together with subsequent pumping by ω_{pump} to $|e\rangle$ changes the state from $|\uparrow, n_x = 2\rangle$ to $|\uparrow, n_x = 1\rangle$. Repeating the procedure thus results in cooling to state $|\uparrow, n_x = 0\rangle$. Due to the narrow linewidth of the $\Delta n_x = -1$ Raman transition, the probability that an atom in the n_x state is excited to $n_x + 1$ is negligibly small, thus repeating the cooling procedure accumulates the atom in the $|\uparrow, n_x = 0\rangle$ state.

4.1.3 Choice of cooling transition

For the ^{87}Rb atom, we chose $|\uparrow\rangle$ to be the meta-stable ground state $|5S_{1/2}, F = 2\rangle$ and $|\downarrow\rangle = |5S_{1/2}, F = 1\rangle$ with a separation $\omega_0 = 6.8$ GHz so that the Raman transition linewidth will not be limited by spontaneous emission from $|\uparrow\rangle$. As spontaneous emission rates are proportional to stimulated emission rates by a factor of a cube of the separation frequency between two internal states [22], the choice of states separated by a microwave frequency thus leads to much smaller spontaneous emission rates opposed to a choice of states separated by an optical frequency.

In principle, we could also use microwave radiation resonant to the magnetic-dipole allowed transition between the two levels to drive the $\Delta n_x = -1$ cooling transition – a single-photon field is definitely easier to setup experimentally than a two-photon field. However, as microwave photons have negligible momentum, they are unable to drive transitions between vibrational states

effectively [31]. We will show in section A.4 that the Rabi frequency of such a transition is reduced by eight orders of magnitude, compared to the same two-level system that is driven by a two-photon Raman transition.

4.2 Sideband Cooling Setup

To control the transfer into the lowest vibrational state, the frequency of the driving fields need to be controlled accurately. In particular, by using a two-photon Raman field to drive transitions between vibrational states, the Raman beam detuning $\omega_0 + \delta_\omega$ must be stable to frequencies much lesser than the two trap frequencies. This is not a difficult technical requirement for microwave frequencies, as opposed to optical frequencies.

The absolute frequency stability of the individual Raman beams are less of a concern as they will be derived from the same laser. Thus the individual frequencies of the Raman beams fluctuate in phase and do not contribute to frequency instability of $\omega_0 + \delta_\omega$. We describe the experimental components creating the Raman beams at frequencies ω_{R1} and ω_{R2} here, where $\omega_{R2} - \omega_{R1} = \omega_0 + \delta_\omega$.

4.2.1 Main Laser

Figure 4.2 illustrates the Raman laser setup. A 780 nm external cavity diode laser (ECDL) is frequency stabilised to ω_C . We intend to derive the Raman beams at ω_{R1} and ω_{R2} from the same beam so that they are phase-coherent with each other. Coarse-frequency stability was ensured by temperature-locking the diode laser chassis, while better than 10 MHz stability was ob-

tained via a digital integrator controlled feedback-loop.

The controller obtains a real-time update of the laser frequency through measuring it with a wavemeter (HighFinesse WS-ultimate). The laser current I and external laser cavity length l which controlled the ECDL laser frequency were the parameters used by the integrator to actively stabilise the frequency to ω_C . Before locking the ECDL to ω_C in order to arrive at a desired Raman detuning Δ_R , we manually scanned the typical values of I and l which we expect the integrator to manipulate during the frequency lock to ensure that the laser frequency varies continuously. This ensures that the laser does not ‘jump’ to another frequency (‘mode-hop’) such that the integrator is unable to restore the laser back to ω_C when I and l are manipulated during the frequency lock.

4.2.2 Creating the Raman beams

To generate the two Raman beams with their frequencies such that ω_{R1} is $2\pi \cdot 6.8 \text{ GHz} + \delta_\omega$ from ω_{R2} , we pass the laser at ω_C through an electro-optic-modulator (EOM) modulated at $2\pi \cdot 6.8 \text{ GHz}$ in the setup shown in Figure 4.3. We split the laser beam at ω_C into two: one part enters a double pass AOM setup adding between 400–410 MHz to ω_C (this becomes the Raman beam 2 laser at frequency ω_{R2}).

The other part of ω_C enters the EOM, which outputs:

$$E(t) = E_c \exp[i(\omega_c t + M \sin \omega_m t)] \quad (4.1)$$

$$= E_c \exp(i\omega_c t) \sum_{n=-\infty}^{+\infty} J_n(M) \exp(in\omega_m t) \quad (4.2)$$

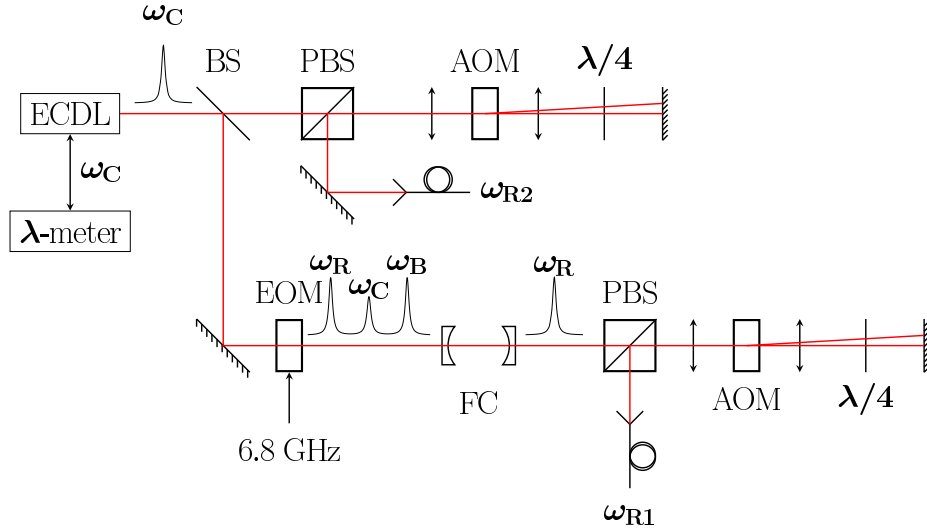


Figure 4.2: Experimental setup for generating Raman pulses. The carrier frequency of an external cavity laser (ECDL) is locked to a wavemeter. One part of the beam is sent through the fast Electro-Optic Modulator (EOM), which adds sidebands at $2\pi \cdot 6.8$ GHz from the carrier ω_C . In order to filter the red sideband (ω_R) from the other frequencies, a low-finesse filter cavity (FC) is used. The red sideband and the carrier are switched on and off with AOMs that also control the two-photon frequency detuning. The beams are then coupled to single mode polarization maintaining fibers and sent to the atom.

E_c, ω_c : Carrier electric field amplitude and angular frequency.

M: Modulation index, proportional to the rf modulation amplitude.

ω_m : rf modulation angular frequency.

By modulating the phase of the input electric field at $\omega_m = 2\pi \cdot 6.8$ GHz, the EOM output field contains frequency sidebands in integer multiples of ω_m . The rf amplitude was adjusted such that the 1st order red-sideband amplitude $J_{-1}(M)$ was maximised.

The EOM was further temperature stabilised to maintain constant output polarization. Polarisation stability is important because the beam passes through polarisation filters before illuminating the atom. The filters convert polarisation instability into intensity instability. As the Rabi oscillation frequency of the Raman transition depends on the intensity of the Raman beams, intensity instability will translate into a time-dependent Rabi frequency, which will manifest as a shorter coherence time of the two-level system.

A low-finesse, fused-silica etalon (finesse ~ 30 , FSR ~ 16.2 GHz, Bandwidth ~ 3.4 GHz) filters the first-order red-sideband $m = -1$ at frequency $\omega_R = \omega_C - \omega_m$, from other frequency components. This is done by tuning the temperature of the cavity, which adjusts its length such that the boundary conditions of the cavity satisfy the resonance condition for transmitting a beam at ω_R . The temperature is then stabilised by a feedback loop to a stability $\delta T < 50$ mK within 5 hours. A low-finesse cavity reduces the transmission fluctuation with respect to cavity length variations which arise due to residual temperature fluctuations still uncompensated for.

The frequency of the ω_R beam was tuned to ω_{R1} by a double-pass AOM setup and focused onto the single-atom. The AOM modulation frequencies of the two AOMs control δ_ω (see fig 4.4.b) that allow us to meet the resonance condition of the $\Delta N_x = -1$ transition. The Raman beams are then coupled through polarization-maintaining fibres and projected onto the atom in the following counter-propagating geometry (see fig 4.3). For this setup, the passive intensity stability of each Raman beam is about 2% within 5 hours.

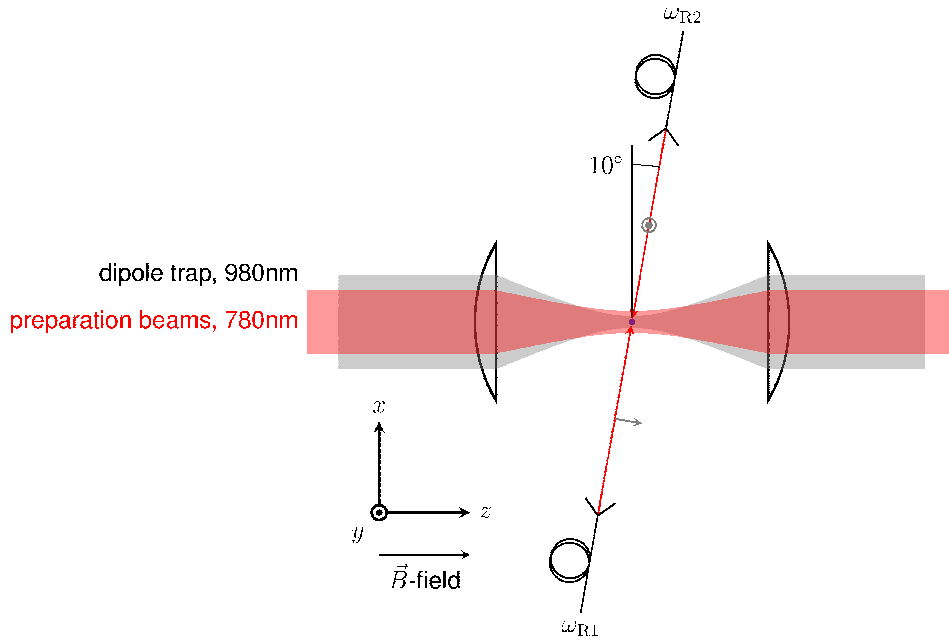


Figure 4.3: Geometry of the Raman beams. An atom is localised in a σ^+ FORT. The trap induces a differential Zeeman sublevel splitting (see fig 4.4) that defines quantisation axis in the z -direction. The Raman beams are sent to the atom such that cooling can be performed for vibrational degrees of freedom in the XZ plane. Raman beam at frequency ω_{R2} polarised along \hat{y} couple (σ^+/σ^-) transitions. A Raman beam at frequency ω_{R1} polarised mainly in the z -axis couple π transitions. The σ^+ and π components perform the Raman transition (see fig 4.4.b). The preparation beams (see fig 4.4.a) co-propagate with the FORT.

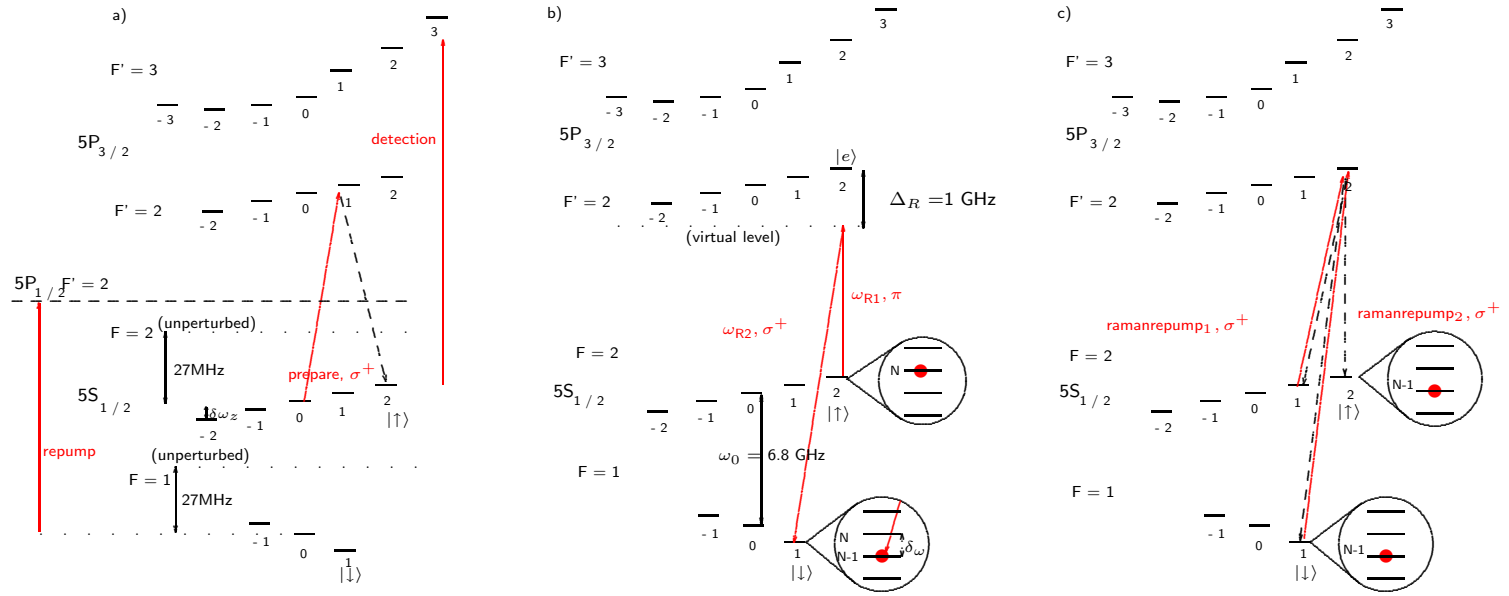


Figure 4.4: Energy level diagram for ^{87}Rb illustrating various qubit operations. Zeeman sublevel splitting is induced by a σ^+ FORT. An additional magnetic field along the quantisation axis augments the differential Zeeman sublevel splitting in the $5S_{1/2}$ manifold to $\delta\omega_z \sim 1.89$ MHz in both $F = 1$ and $F = 2$ manifolds. An AC Stark shift of the $5S_{1/2}$ manifold creates a trap depth of $U_0 = h \cdot 27$ MHz. (a) The red arrows pointing from the $F = 1$ and $F = 2$ manifolds illustrates the initialisation step. Black arrows indicate spontaneous emission. Applying σ^+ light tuned to the preparation transition pumps the population towards the $|\uparrow\rangle$ qubit state. The repump transition evacuates the population from the $F = 1$ manifold. State detection is performed by high-intensity MOT beams that kick an atom prepared in $|\uparrow\rangle$ out of the trap, then checking for the presence of a single scatterer with low-intensity MOT beams. (b) Two laser beams detuned from the excited state and with frequency difference tuned to the hyperfine splitting $\omega_0 = 6.8$ GHz drive the stimulated Raman transitions. These transitions can create any arbitrary superposition of the qubit states. To reduce the motional level from N_x to $N_x - 1$, the Raman beams are further detuned to $\omega_{R2} - \omega_{R1} = \omega_0 + \delta_\omega$ such that $\delta_\omega = \omega_x$. (c) To repeat the cooling procedure in (b), two ‘Ramanrepump’ beams pump the atom exclusively into the $|\uparrow, N_x - 1\rangle$ state. Since the recoil energy of the atom due to one repump photon $\approx h \cdot 6.8$ kHz $\ll \hbar\omega_x = h\omega_x = h \cdot 80$ kHz, the motional quanta $N_x - 1$ is unlikely to change during spontaneous emission. Details in Section 4.3.

4.3 Resolved-sideband Raman Cooling Cycle in ^{87}Rb

We trap a single atom with the same procedure as described in Chapter 2: An atom is loaded into the FORT by the MOT, comprising of the MOT beams and the quadrupole magnetic field produced by the MOT coils. Optical molasses cooling for 20 ms by the MOT beams removes kinetic energy from the trapped atom, such that its Maxwell-Boltzmann energy distribution probability is one that is characterised by a temperature at $35\ \mu\text{K}$.

The detailed level schemes for the Raman cooling cycle are shown in Figure 4.4. The Raman cooling cycle begins with optical pumping into $|\uparrow\rangle$ (fig 4.4.a). The optical pumping transitions were performed by two beams (**preparation beams**): the preparation beam driving $|5S_{1/2}, F = 2\rangle \rightarrow |5P_{3/2}, F' = 2\rangle$ σ^+ transition and the repump beam driving the $|5S_{1/2}, F = 1\rangle \rightarrow |5P_{1/2}, F' = 2\rangle$ transition². When the atom is prepared in $|\uparrow\rangle$, it becomes decoupled from the σ^+ preparation and repump beams. Unlike the state preparation procedure for the extinction experiment, we do not use the σ^+ transition from $|F = 2\rangle \rightarrow |F' = 3\rangle$ because the atom in $|\uparrow\rangle$ will enter into a closed-cyclic transition ($|\uparrow\rangle \leftrightarrow |F' = 3, m'_F = 3\rangle$) under the σ^+ preparation fields. This causes the atom to continually scatter photons, gaining recoil energy.

Two monochromatic beams at frequencies ω_{R1} and ω_{R2} (fig 4.4.b) off-resonant by Δ_R from $|e\rangle$ drive the Raman transition between $|\uparrow\rangle$ and $|\downarrow\rangle$. To

²Unless otherwise stated unprimed variables F and m_F refer to $5S_{1/2}$ sublevels while primed variables F' and m'_F refer to $5P_{3/2}$ sublevels.

ensure that the population in $|\uparrow\rangle$ and $|\downarrow\rangle$ do not leak to neighbouring m_F states, a magnetic field bias along \hat{z} augments the existing ³ Zeeman sublevel splitting between adjacent m_F levels in the $5S_{1/2}$ manifold from ~ 300 kHz to ~ 1.89 MHz.

In the harmonic FORT potential, the internal states are dressed with vibrational states spaced $(\omega_z, \omega_x, \omega_y)$ apart, corresponding to the FORT trap frequencies. When the two-photon detuning is set such that $\delta_\omega < 0$ and δ_ω coincides with the trap frequency ω_x (ω_z), the motional quanta N_x (N_z) decreases by one.

For example, to remove one motional quanta from x-axis oscillator, a π -pulse at

$$t_\pi = \pi/\Omega_{N_x-1, N_x} \quad (4.3)$$

completely transfers the population from $|\uparrow, N_x\rangle$ to $|\downarrow, N_x - 1\rangle$ (see Section A.4 for the expression for the Rabi frequency Ω_{N_x-1, N_x}). For the π -pulse to resolve the vibrational levels in the x-axis harmonic oscillator, the application time t_π must significantly exceed the oscillation period $2\pi/\omega_x$.

To repeat the Raman transition, we re-initialise the atom into $|\uparrow\rangle$ (fig 4.4.c). Two beams, ramanrepump₁ and ramanrepump₂ drive spontaneous Raman cycles that pump the atom back into $|\uparrow, N_x - 1\rangle$. Once the atom is pumped into $|\uparrow, N_x - 1\rangle$, it is decoupled from these beams. Thus we do not have to be too concerned with overexposing the atoms to these beams.

The state $|F' = 2, m'_F = 2\rangle$ state was chosen to be the excited state of these spontaneous Raman transitions as the $|F' = 2, m'_F = 2\rangle \rightarrow |F = 2, m_F = 2\rangle$

³The σ^+ FORT also causes differential Zeeman AC Stark shifts between the magnetic sublevels of the hyperfine states.

π -transition amplitude is the largest compared to the transitions $|F' = 2, m'_F = 1\rangle \rightarrow |F = 2, m_F = 2\rangle$ or $|F' = 1, m'_F = 1\rangle \rightarrow |F = 2, m_F = 2\rangle$.⁴

This pulse sequence (fig. 4.4b. and c.) is repeated many times until the atom reaches the vibrational ground state, which does not respond any longer to vibrational level-reducing transitions.

4.4 Coherence time measurements

An inherent requirement of the cooling scheme is that the internal states remain coherent within the application of several Raman cooling π -pulses (see fig 4.4.b), each being much longer than the trap oscillation period such that the vibrational levels are resolved. To resolve vibrational levels of the harmonic oscillator in the x and z axes, the lower limit to the coherence time is:

$$t_C \gg t_\pi \gg \text{Max}\{2\pi/\omega_z, 2\pi/\omega_z\} = 2\pi/\omega_z = \frac{1}{13 \text{ kHz}} \approx 70 \mu\text{s} \quad (4.4)$$

Ramsey spectroscopy on a similar near-micron sized dipole trap (oscillation frequencies 125 kHz, 23 kHz) on a two-level clock transition via two-photon Raman transitions by Grangier et al. [32] measured a dephasing time of 370 μs . However, their Raman beams were in a co-propogating geometry and the transition was thus not Doppler-broadened. Thus in the counter-propogating geometry for our case, we would expect to yield a smaller dephasing(decoherence) time. Nonetheless, at least in a Doppler-insensitive

⁴The transition amplitude values for ⁸⁷Rb are readily available from [29].

configuration, 370 μs seems much longer than the prerequisite 70 μs , so there is hope.

4.4.1 Rabi oscillation

The first step to observe Raman transitions is to drive a transition which affects the internal state of the atom, and not be too concerned with the vibrational state as this would require one to experimentally determine the resonance condition δ_ω to a precision of kHz. This poses a challenge initially because the FORT introduces AC Stark shifts that perturb the frequency separation between the driven states to the order of MHz, but the theoretical predictions of these shifts require knowledge of the various electric dipole transition amplitudes of ^{87}Rb (see Section A.5), that vary significantly between several databases [2]. Thus we were only able to predict an accurate value for δ_ω up to several MHz.

As such we first drive the Raman transition at short time scales such that the absorption linewidth is about 1 MHz, allowing us to vary δ_ω at steps of 1 MHz until we observe that the Raman fields drive the $|\uparrow\rangle \rightarrow |\downarrow\rangle$ transition. The idea is that once we arrive at this ‘coarse’ value of δ_ω , we may repeat the above procedure for a more precise value of δ_ω by using longer time scale Raman pulses.

The experimental sequence for observing Rabi oscillation of the population in $|\downarrow\rangle$ after undergoing the two-photon Raman transition for variable time t is as follows:

Figure 4.5 summarises the experimental sequence: (Cooling and loading)

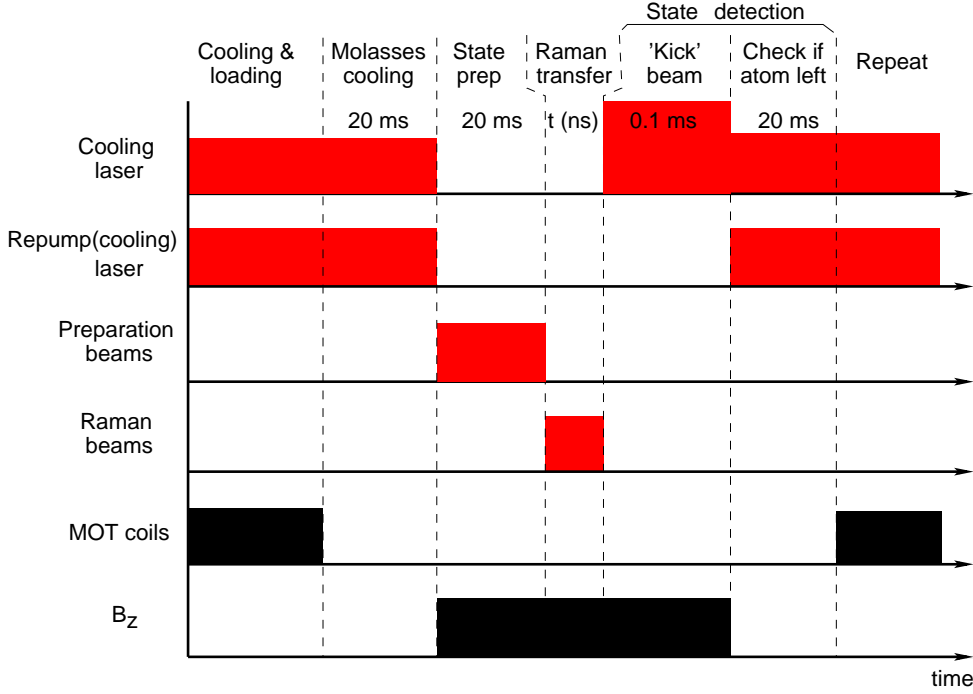


Figure 4.5: Schematic of the temporal sequence for recording the Rabi oscillation of the population in $|\downarrow\rangle$ undergoing Raman transition. Details in text.

The MOT beams and coils create the MOT which loads the FORT. (Molasses cooling) Once loading in the FORT is detected, the atom is subjected to 20 ms of optical molasses cooling by the MOT beams. (State preparation) The atom is first prepared in $|\uparrow\rangle$ by the preparation beams (see fig 4.4.a). (Raman transfer) The Raman beams are then turned on for variable time t . A static magnetic field along the quantisation axis could be turned on to augment differential Zeeman sublevel splitting in the $5S_{1/2}, F = 1$ and $5S_{1/2}, F = 2$ manifolds such that only $|\uparrow\rangle$ and $|\downarrow\rangle$ are the only magnetic substates in these manifolds that are coupled to the Raman beams.

State detection is done by i) subjecting the atom to the MOT cooling laser already near-resonance to $|F = 2\rangle \rightarrow |F' = 3\rangle$ transition(see fig 4.4.a).

The beam intensity is increased at this stage, such that it kicks an atom in state $|\uparrow\rangle$ out from the FORT. Conversely, an atom in state $|\downarrow\rangle$ will be decoupled to this beam. Thus we effectively map the internal state onto the presence of the atom in the trap. ii) To infer the internal state from the presence of the atom in the trap, we illuminate it with less intense MOT beams and look for fluorescence photons above background counts.

To repeat the experiment on another atom, any atom present in the FORT from this point is released by turning off the FORT for 500 μs and we restart the MOT again in order to load a ‘fresh’ atom. We cannot reuse the atom in the trap because it is now in state $|\downarrow\rangle$ but we want an atom in the initial state $|\uparrow\rangle$ to begin the Raman transition with. We record the fraction of events for which the atom remains in the trap, subject to a standard-error of 3%. This corresponds to the probability P_{\downarrow} that the atom was in $|\downarrow\rangle$.

The above procedure was repeated for several Raman transition detunings $\omega_0 + \delta_\omega$ until maximum visibility of the population oscillation was obtained. The calculated differential AC Stark shift between $|\uparrow\rangle$ and $|\downarrow\rangle$ due to the FORT was taken as the initial value of δ_ω .

As a preliminary measurement, the Raman beam intensities and detunings were adjusted to achieve Raman Rabi frequencies in the order of 1 MHz, which we supposed would allow us to observe several Rabi oscillations, as we expected the coherence time to be of the order of μs .

4.4.2 Results

Figure 4.6 shows the Rabi oscillation of the $|\downarrow\rangle$ occupation probability P_{\downarrow} with respect to the duration of the Raman pulse. It is clear that by increasing the differential Zeeman splitting of the $F = 1$ and $F = 2$ manifolds from $\delta\omega = 300$ kHz (fig 4.6, top) to $\delta\omega = 1.89$ MHz (fig 4.6, bottom), the Rabi oscillations decay more slowly. Without the Zeeman splitting, for Rabi oscillations at $\Omega_R \approx 2\pi \cdot 1.0$ MHz the coherence time was measured to be ~ 0.4 μ s. With Zeeman splitting, we obtained for $\Omega_R \approx 2\pi \cdot 1.3$ MHz an extended coherence time of ~ 3.3 μ s.

In the process of increasing the number of Rabi oscillations, we also increased the detuning Δ_R from $2\pi \cdot 160$ MHz (top) to $2\pi \cdot 1$ GHz (bottom), such as to decrease the number of scattered photons from $|e\rangle$ by about six times. The two-photon Raman transition Rabi frequency Ω_R is directly proportional to $E_{R1} \cdot E_{R2} / \Delta_R$ (see Equations A.15 and A.21) while the scattering rate R_{scatt} on transition $|\uparrow\rangle \rightarrow |e\rangle$ (see fig 4.4.b) is approximately $\Gamma \cdot E_{R1} \cdot E_{R2} / \Delta_R^2$ [16], where $\Gamma \approx 2\pi \cdot 6$ MHz is the linewidth of the $|\uparrow\rangle \rightarrow |e\rangle$ transition. Thus in t_{π} we would expect the number of scatterings to be $N_{scatt} = R_{scatt} \cdot \frac{\pi}{\Omega_R} \propto \Gamma / \Delta_R$ [16]. For the two Rabi oscillation curves of approximately the same Rabi frequency, the ratio of the number of spontaneous emission events within t_{π} is approximately $160/1000 \approx 0.16$.

4.4.3 Increasing coherence time

Another source of decoherence is from ambient magnetic fields that affect the magnetically-sensitive states used for the Raman transition [30]; a magnetic

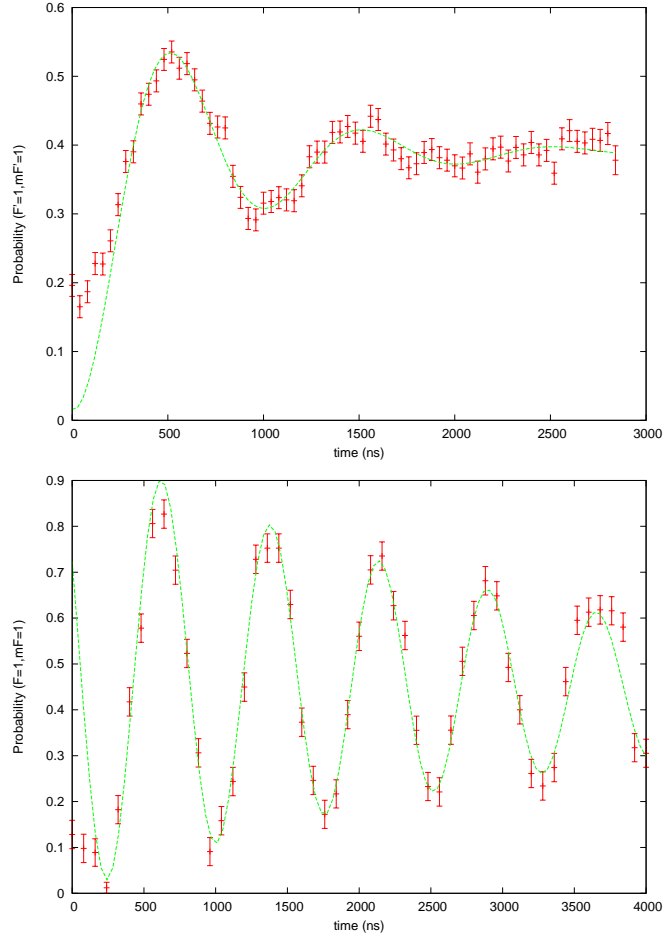


Figure 4.6: Rabi oscillation curves showing $|\downarrow\rangle = |F = 1, m_F = 1\rangle$ population occupation probability versus application time of the Raman pulse. (Top) Differential Zeeman sublevel splitting of the ($F = 1$) and ($F = 2$) hyperfine structure was at $\delta\omega_z \sim 300$ kHz (see fig 4.4), caused by AC Stark effect of a σ^+ FORT. At pulse times shorter than $1/(300 \text{ kHz})$, ($|\uparrow\rangle \leftrightarrow |\downarrow\rangle$) is not the only transition that can be driven by the Raman fields. This results in leakage of the population in $|\downarrow\rangle$ to other m_F levels in the ($F = 1$) and ($F = 2$) manifold by the Raman beams and thus a rapid decay of the Rabi oscillation. A coherence time of $0.4\mu\text{s}$ was measured. The detuning from the excited level was $\Delta_R = 160$ MHz. (Bottom) Differential Zeeman sublevel splitting was augmented to $\delta\omega_z \sim 1.89$ MHz by static magnetic field along the quantisation axis. This allows the Raman beams to be resonant only to the two-level transition ($|\uparrow\rangle \leftrightarrow |\downarrow\rangle$), resulting in slower decay of the Rabi oscillation. The detuning was increased to $\Delta_R = 1$ GHz while adjusting the Raman beam intensities to achieve about the same Rabi frequency. For both curves, the data points taken before 250 ns deviated from a decaying exponential sinusoidal model (green curves), presumably due to the finite rise and shut-off times of the Raman beams.

field orthogonal to the quantisation axis causes the atom to undergo Larmor precession, leaking population from $|\uparrow\rangle$ or $|\downarrow\rangle$ to other m_F states, which upsets the clean two-level system [1]. Furthermore, fluctuating magnetic fields couple to magnetically sensitive states, introducing phase decoherence. To circumvent this, a ‘clock’ transition can be used (see fig 4.7). This is done by using $|\uparrow\rangle = |F = 2, m_F = 0\rangle$ and $|\downarrow\rangle = |F = 1, m_F = 0\rangle$ magnetically-insensitive Zeeman substates. Preparation to the new state $|\uparrow\rangle$ can be done by a pair of preparation beams (see fig 4.4.a) with polarizations adjusted to excite π -transitions from the two hyperfine states of $5S_{1/2}$ to the excited state manifold ($5P_{3/2}, F' = 2$)⁵. The Raman cooling scheme utilising clock transitions is proposed in fig 4.7.

⁵The π -pumping works because $|\uparrow\rangle$ is the only state in the $F = 1$ and $F = 2$ manifolds that is decoupled from the preparation beams, while spontaneous emission from the $F'=2$ manifold can decay into $|\uparrow\rangle$.

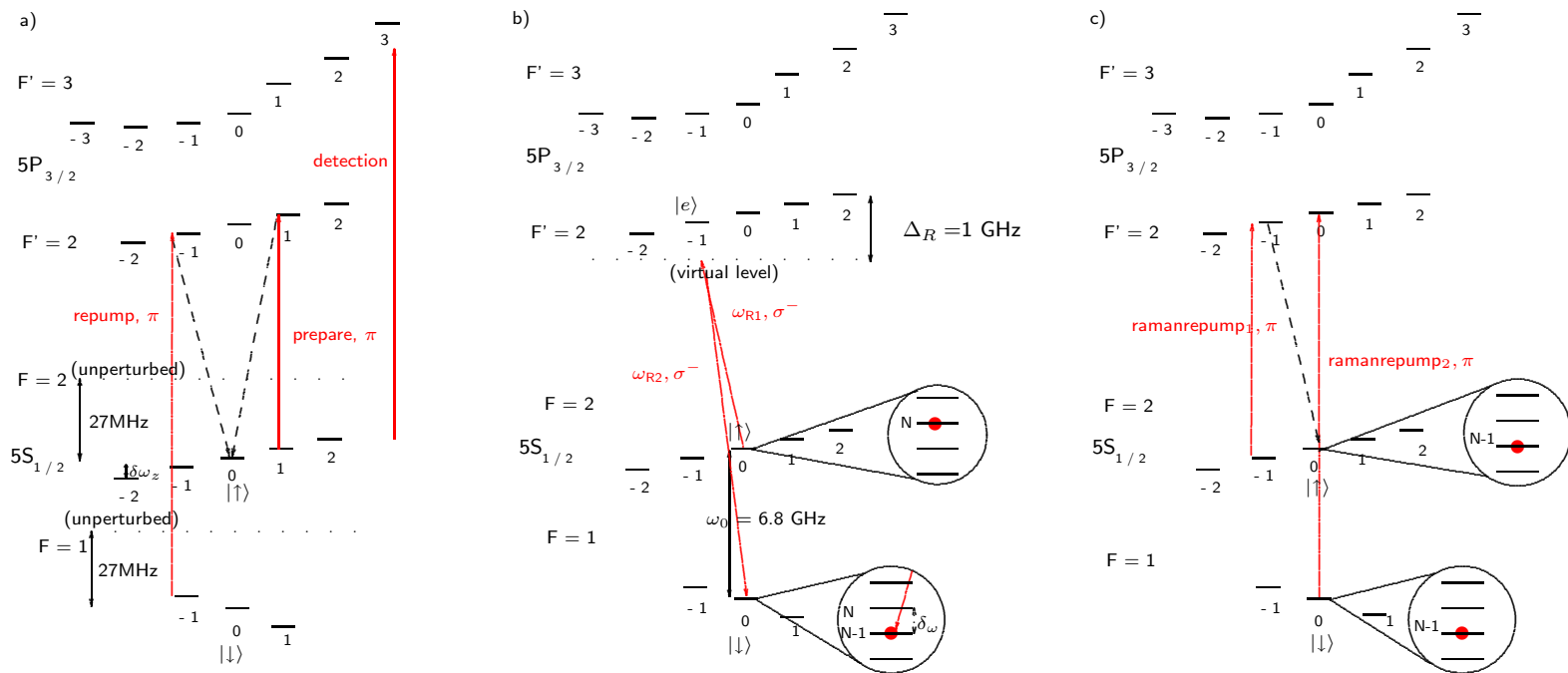


Figure 4.7: Energy level diagram for ^{87}Rb illustrating various qubit operations involving clock states. (a) State initialisation to $|\uparrow\rangle = |F=2, m_F=0\rangle$ is via two π beams (red arrows) coupling manifolds $F=1$ and $F=2$ to the $F'=2$ manifold. (b) Two Raman laser beams detuned from the $F'=2$ manifold drive the stimulated two-photon transition. σ^- beams are used instead of π beams as the π transition amplitude of $|\uparrow\rangle \rightarrow |e\rangle$ vanishes. (c) Raman-recycling beams optically pump the atom back into $|\uparrow\rangle$. Details in Section 4.4.3

In the experimental setup, we may obtain a σ^- beam at ω_{R1} (see fig 4.7.b) by altering the existing setup originally illustrated in Figure 2.1.

1. Replacing the first mirror encountered by the probe beam by a PBS (see fig 2.1) which acts as a mirror when the polarization of the light exiting the probe coupler is adjusted vertical.
2. Delivering a H-polarised light at ω_{R1} into this new PBS such that it co-propagates with the σ^+ probe beam. The HWP and QWP that follow after this new PBS converts this light into circular polarisation corresponding to a σ^- beam.

A σ^- beam at ω_{R2} can still be supplied by the \hat{y} -polarised beam (see fig 4.3) which has both σ^+ and σ^- components. The π -preparation beams correspond to linearly polarised light along the quantisation axis along \hat{z} . We may propagate it to the atom along the x-direction. Unfortunately, due to time constraints the Rabi oscillation curve for the clock transition was not obtained.

4.5 Outlook

Once the condition for long coherence time ($\tau_C \gg 70 \mu\text{s}$) is met, the motional sidebands can be resolved by the two-photon Raman transition. One could drive the Raman transition at a fixed time τ and sweep through a range of values of δ_ω such that the two-photon Raman detuning meets the resonance condition for various $|\uparrow, N_x, N_y, N_z\rangle \rightarrow |\uparrow, N'_x, N'_y, N'_z\rangle$ transitions. In particular, we can obtain the experimental value for the on-resonant Raman

detuning frequency ($\delta_\omega = \omega_x$) when the $\Delta N_x = -1$ cooling transition takes place.

In the event when the coherence time cannot be extended such as to resolve the motional sideband Raman transitions, alternate cooling schemes suggested in the concluding chapter could be explored.

Conclusions and Outlook

In this thesis, we characterised the energy distribution of a laser cooled single ^{87}Rb atom in a far-off resonant dipole trap (FORT). This is done by determining the probability $P_{RR}(\Delta t)$ of recapturing the atom by the FORT after the atom is released by shutting off the FORT for a variable time Δt – an atom with a higher average kinetic energy will have a lower overall recapture probability. Using a classical treatment of the atomic motion, and assuming a Maxwell-Boltzmann distribution, we determine the average energy to correspond to a temperature $T = 35(1) \mu\text{K}$.

Alternatively, we may treat the atomic motion quantum mechanically, in which the atom occupies some superposition of several Fock number states $|n_x, n_y, n_z\rangle$ of the confining harmonic potential. The quantum treatment approaches the classical treatment for large \bar{n}_j , $j \in \{x, y, z\}$. The temperature T determined in our experiment corresponds to $\bar{n}_x = \bar{n}_y = 8.6$ and $\bar{n}_z = 55.6$. Thus, treating the atomic motion classically may not be valid, and a more sophisticated treatment is necessary:

To determine more accurately \bar{n}_j , we could adopt an experimental method called sideband thermometry [30]. It essentially utilises the asymmetry in transfer probability in driving the $|n_j\rangle \rightarrow |n_j + 1\rangle$ transition versus the

$|n_j\rangle \rightarrow |n_j - 1\rangle$ transition to determine \bar{n}_j . The driven transition is a two-photon Raman transition similar to that used for resolved-sideband Raman cooling (see Section [?]). The implicit requirement is that the coherence time t_C of the involved transitions is much longer than the pulse duration of the Raman beams used to drive the transition. The pulse duration in turn, has to be long enough to resolve the motional levels of our trap. To resolve the motional levels that dress the internal states of the atom at 80 kHz and 13 kHz, we require t_C to be at least 70 μs .

In this work, we also demonstrated Rabi oscillation between two hyperfine ground states of the atom using a two-photon Raman transition, which would be the starting point of a cooling scheme that should bring the atom close to its motional ground state. So far, we could achieve a Rabi frequency of 1.3 MHz and observed a coherence time $t_C = 3.3 \mu\text{s}$. Increasing t_C above 70 μs in our setup is required if we want to adopt a cooling procedure that resolves the motional levels so as to optically transfer the atom down one motional level at a time (resolved-sideband Raman cooling).

Cooling the atom to its motional groundstate was motivated by the fact that a well-localised atom has been shown in Tey's [2] extinction experiment to be a more effective scatterer of light. In Tey's experiment, the ^{87}Rb is prepared in the $(5S_{1/2}, F = 2, m_F = 2)$ groundstate and is driven by a σ^+ 'probe' beam to $(5P_{3/2}, F' = 3, m'_F = 3)$, simulating a driven closed two-level system. The extinction corresponds to the ratio of the probe light collected after being scattered by the atom as compared to the probe light collected when the atom is absent.

In the event that t_C cannot be increased with the method suggested in

Section 4.4.3, we could explore the following alternative techniques in order to perform the extinction experiment on an ensemble of atoms with a lower mean kinetic energy: i) by adiabatically lowering and raising of the trapping potential, we release the more energetic atoms [3], and ii) Raman cooling but without resolving the vibrational levels of the atom in the trap [33]. We briefly comment on each technique.

Adiabatic lowering and raising of trap potential: By decreasing the trap depth adiabatically, the occupation probabilities of the vibrational levels are preserved. For an ensemble of similarly trapped single atoms whose energies obey a thermal distribution, there will be instances when a highly energetic atom with an initial energy E_i in an initial trap depth U_i will eventually have an energy E_{esc} that is equal to the final trap depth U_{esc} such that the atom escapes [3]. To proceed with the extinction experiment, the trap is then adiabatically restored to its original depth, such that in the event when a less energetic atom remains in the FORT, its energy could be returned to its original value. We then measure the probe extinction, subsequently checking for the presence of the atom in the trap. The data for the probe extinction is then post-selected for atoms which remain loaded. This process is similar to the evaporative cooling technique typically performed with many atoms [34] but because it is performed on a single atom, there is no collision-induced rethermalization [3] - no cooling takes place when the trap depth is lowered and restored adiabatically to its original value. Rather, this process acts as a filter allowing a more energetic atom to escape, while an atom with a lower kinetic energy remains. This allows the extinction of the probe beam to be measured only in instances where a less energetic atom is loaded in the

single-atom trap.

Raman cooling: Raman cooling of atoms without resolving the vibrational levels of their trapping potential is performed quite differently from the sideband-resolved Raman cooling described in this work. A pair of counter-propagating Raman beams is used to drive the transition between two internal ground states, imparting $2\hbar k$ of momentum. The upper state is chosen as a meta-stable state that is so long lived that the linewidth γ of the Raman transition is essentially only limited by the duration t_π of the transition. In the rest-frame of the atom, the Raman beams are Doppler shifted in frequency such that by adjusting the frequency difference δf of the Raman beams, one may drive the two-photon Raman transition only for atoms with a particular velocity. For transitions of long duration, the transition linewidth is so narrow that it becomes extremely velocity selective. Thus, Raman pulses can be tailored such that they do not excite atoms whose velocity is already near $v = 0$. The Raman transition is followed by an optical pumping pulse that returns the atom to its original state before the Raman transition. Due to the spontaneous emission process in the pumping procedure, the velocity of the atom is randomised such that for some finite probability, the velocity of the atom is pushed towards $v = 0$. By repeating this sequence for several δf and t_π followed by an optical pumping pulse, one may excite an adjustable width of velocities around a specific velocity class such that atoms are gradually accumulated in a narrow velocity space around $v = 0$ [35].

This cooling method has been demonstrated for atoms in free space loaded initially from a magneto-optical trap [36], and also for atoms in a blue-detuned dipole force trap whose large volume enables atoms to main-

tain a relatively constant velocity over the time-scale of a typical Raman transition [37]. In a high-axial frequency dipole trap, the atomic oscillation frequency approaches the two-photon Raman Rabi frequency. This implies that the range of velocities during the two-photon π transition is extremely broad, thus broadening the velocity selective transitions used for the Raman cooling scheme, reducing cooling performance [37].

As $t_C = 3.3 \mu\text{s}$, the smallest linewidth of the Raman pulse is $\sim 300 \text{ kHz}$. This means that the upper limit to the smallest vibrational level in the trap which can be decoupled from the Raman beam is about $n_\rho = 2\pi \cdot 300 / \omega_\rho = 300/80 \approx 3.8$. This is still smaller than the current average vibrational quanta of $n_\rho = 8.6$, though not at the ground state of the trap.

To bridge this cooling scheme for the extinction experiment, we can perform a velocity selective Raman transition for velocities around $v = 0$ into the initial state $|5S_{1/2}, F = 2, m_F = 2\rangle$ for the probe transition after Raman cooling. Velocity selection is necessary as the Raman cooling scheme is performed repeatedly on a single atom and a finite probability exist for the atom to be heated by the cooling sequence instead of being cooled, due to the randomisation of velocities by the aforementioned optical pumping pulse. The probe transmission is then measured followed by a check for the presence of the atom. The data for the transmission is then post-selected for atoms present in the trap.

Bibliography

- [1] Tey, M. K. *et al.* Strong interaction between light and a single trapped atom without a cavity. *Nature Physics* **4**, 924–927 (2008).
- [2] Khoon, T. M. *Interfacing Light and a Single Quantum System with a Lens*. Ph.D. thesis, National University of Singapore (2008).
- [3] Tuchendler, C., Lance, A. M., Browaeys, A., Sortais, Y. R. P. & Grangier, P. Energy distribution and cooling of a single atom in an optical tweezer. *Physical Review A* **78** (2008).
- [4] Cirac, J. I., Zoller, P., Kimble, H. J. & Mabuchi, H. Quantum state transfer and entanglement distribution among distant nodes in a quantum network. *Physical Review Letters* **78**, 3221–3224 (1997).
- [5] Duan, L. M., Lukin, M. D., Cirac, J. I. & Zoller, P. Long-distance quantum communication with atomic ensembles and linear optics. *Nature* **414**, 413–418 (2001).
- [6] Matsukevich, D. N., Maunz, P., Moehring, D. L., Olmschenk, S. & Monroe, C. Bell inequality violation with two remote atomic qubits (2008).
- [7] Blinov, B. B., Moehring, D. L., Duan, L. M. & Monroe, C. Observation of entanglement between a single trapped atom and a single photon. *Nature* **428**, 153–157 (2004).
- [8] Volz, J. *et al.* Observation of entanglement of a single photon with a trapped atom. *Physical Review Letters* **96**, 030404 (2006).
- [9] Savage, C. M., Braunstein, S. L. & Walls, D. F. Macroscopic quantum superpositions by means of single-atom dispersion. *Opt. Lett.* **15**, 628 (1990).
- [10] Meschede, D., Walther, H. & Müller, G. One-atom maser. *Physical Review Letters* **54**, 551–554 (1985).

- [11] Turchette, Q. A., Hood, C. J., Lange, W., Mabuchi, H. & Kimble, H. J. Measurement of conditional phase shifts for quantum logic. *Phys. Rev. Lett.* **75**, 4710–4713 (1995).
- [12] Pinkse, P. W. H., Fischer, T., Maunz, P. & Rempe, G. Trapping an atom with single photons. *Nature* **404**, 365–368 (2000).
- [13] Boozer, A. D., Boca, A., Miller, R., Northup, T. E. & Kimble, H. J. Reversible state transfer between light and a single trapped atom. *Physical Review Letters* **98**, 193601 (2007).
- [14] Gleyzes, S. *et al.* Quantum jumps of light recording the birth and death of a photon in a cavity. *Nature* **446**, 297–300 (2007).
- [15] Pinkse, P. W. H., Fischer, T., Maunz, P. & Rempe, G. Trapping an atom with single photons. *Nature* **404**, 365–368 (2000).
- [16] Foot, C. J. *Atomic physics* (Oxford University Press, Oxford, 2005).
- [17] Tey, M. K. *et al.* Interfacing light and single atoms with a lens. *New Journal of Physics* **11**, 043011 (2009).
- [18] Teo., C. *Coupling of focused light to single atom*. Master’s thesis, NUS (2010).
- [19] M. Weidemüller & Zimmerman, C. *Cold atoms and molecules* (Wiley, 2009).
- [20] Schlosser, N., Raymond, G. & Grangier, P. Collisional blockade in microscopic optical dipole traps. *Phys. Rev. Lett.* **89**, 023005 (2002).
- [21] Kuppens, S. J. M., Corwin, K. L., Miller, K. W., Chupp, T. E. & Wieman, C. E. Loading an optical dipole trap. *Phys. Rev. A* **62**, 013406 (2000).
- [22] Bransden, B. & Joachain, C. *Physics of atoms and molecules* (Prentice Hall, 2003).
- [23] Lett, P. D. *et al.* Observation of atoms laser cooled below the doppler limit. *Phys. Rev. Lett.* **61**, 169–172 (1988).
- [24] A Fuhrmanek, A. M. L., Tuchendler, C., P Grangier, Y. R. P. S. & Browaeys, A. Imaging a single atom in a time-of-flight experiment (2010).

- [25] Bücker, R. *et al.* Single-particle-sensitive imaging of freely propagating ultracold atoms. *New Journal of Physics* **11**, 103039 (2009).
- [26] Bevington, P. R. & Robinson, D. K. *Data reduction and error analysis for the physical sciences* (McGraw-Hill, New-York, 2003).
- [27] Poli, N., Brecha, R. J., Roati, G. & Modugno, G. Cooling atoms in an optical trap by selective parametric excitation. *Phys. Rev. A* **65**, 021401 (2002).
- [28] Adams, C. S. & Riis, E. Laser cooling and trapping of neutral atoms. *Progress in Quantum Electronics* **21**, 1–79 (1997).
- [29] Steck, D. Rubidium 87 d line data. URL <http://steck.us/alkalidata>. Accessed on Nov 2007.
- [30] Louis, D. *Cooling and Heating of the Quantum Motion of Trapped Cadmium Ions*. Ph.D. thesis, University of Maryland (1996). URL www.iontrap.umd.edu/publications/archive/Thesis_2006_Deslauries.pdf.
- [31] Förster, L. *et al.* Microwave control of atomic motion in optical lattices (2009). URL <http://arxiv.org/abs/0909.0678>. 0909.0678.
- [32] Jones, M. P. A. *et al.* Fast quantum state control of a single trapped neutral atom. *Phys. Rev. A* **75**, 040301 (2007).
- [33] Lee, H. J. *et al.* Dipole trapping, cooling in traps and long coherence times. *Atomic Physics* **14** (1994).
- [34] Luiten, O. J., Reynolds, M. W. & Walraven, J. T. M. Kinetic theory of the evaporative cooling of a trapped gas. *Phys. Rev. A* **53**, 381–389 (1996).
- [35] Grimm, R., Weidemüller, M. & Ovchinnikov, Y. B. Optical dipole traps for neutral atoms. *MOLECULAR AND OPTICAL PHYSICS* **42**, 95 (2000).
- [36] Kasevich, M. & Chu, S. Laser cooling below a photon recoil with three-level atoms. *Physical Review Letters* **69**, 1741 (1992).
- [37] Lee, H. J., Adams, C. S., Kasevich, M. & Chu, S. Raman cooling of atoms in an optical dipole trap. *Phys. Rev. Lett* **76** (1995).
- [38] Sakurai, J. J. *Modern Quantum Mechanics* (Addison-Wesley, 1994).

- [39] Sobelman, I. I. *Atomic Spectra and Radiative Transitions* (Springer, 1979).
- [40] Weisskopf, V. & Wigner, E. *Z. Phys.* **63**, 54 (1930).
- [41] Loudon, R. *The Quantum Theory of Light* (Oxford University Press, Oxford, 1973).
- [42] NIST. National institute of standards and technology physical reference data. URL <http://physics.nist.gov/PhysRefData/ASD/index.html>. Accessed on Jun 2007.
- [43] Smith, P. L., Heise, C., Esmond, J. R. & Kurucz, R. L. Amp tools: Databases: Kurucz atomic line database. URL <http://www.cfa.harvard.edu/amp/ampdata/kurucz23/sekur.html>. Accessed on Mar 2009.
- [44] Leibfried, D., Monroe, C., Blatt, R. & Wineland, D. Quantum dynamics of single trapped ions. *Review of Modern Physics* **75**, 281 (2003).
- [45] Abramowitz & Stegun. *Handbook of Mathematical Functions* (U.S. Govt Printing Office, Washington D.C., 1964).

Appendix A

A.1 The D1 and D2 transition hyperfine structure of the ^{87}Rb atom

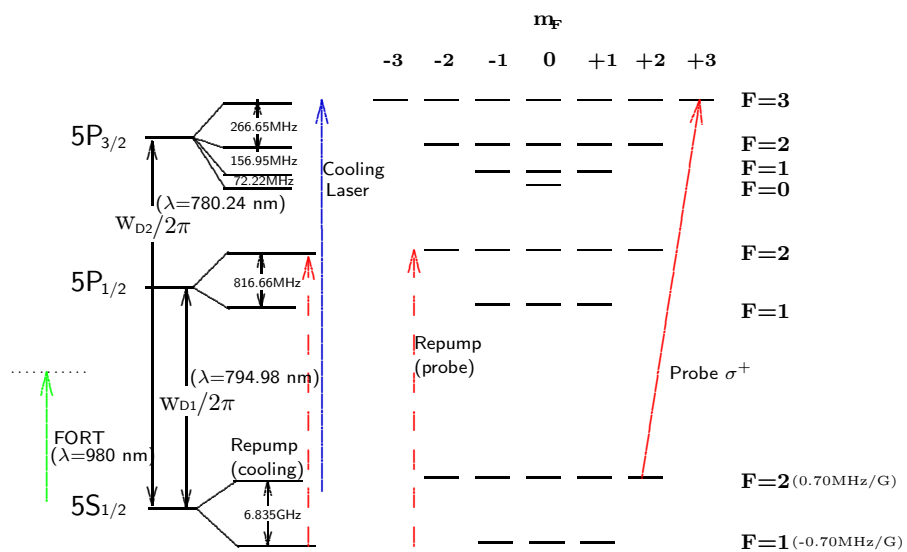


Figure A.1: Hyperfine structure of the D1 and D2 transition for the ^{87}Rb atom, with frequency splittings between the hyperfine levels. The transitions we used for the MOT are shown. Zeeman splittings between adjacent magnetic sublevels are shown for the hyperfine ground states.

A.2 FORT characteristics

This section consolidates the equations used to calculate the AC Stark shift of the ^{87}Rb atomic energy levels, characterises the FORT trap frequencies and explains the choice of the FORT polarization.

One way to qualitatively understand the trapping mechanism in the FORT is to first look at the perturbation of the atomic energy levels by the FORT light. Since the perturbation is intensity-dependent (see Section A.2.1), a spatial distribution of the FORT intensity therefore translates into position-dependent energy eigenvalues.

The FORT (980 nm) used in our experiment is red-detuned from the D1 (795 nm) and D2 (780 nm) transitions of ^{87}Rb , thus creating a negative energy shift for the $5S_{1/2}$ groundstate manifold (see Section A.2.1). The atom is mostly in this manifold unless excited so it usually assumes a negative potential in the FORT. For a Gaussian beam, the intensity gradient at any position is directed towards the location of maximum field strength. This translates into an energy gradient and hence a force which confines the atom to that location (see fig 2.1).

A.2.1 AC Stark shift

Discussions on time-dependent perturbation theory and AC Stark shifts can be found in [38, 29, 22]. Here we consolidate the formulas used to predict the AC Stark shift $\Delta E(F, m_F)$ of some internal state $|F, m_F\rangle$ of the atom in the FORT. We will work in the regime where $\Delta E(F, m_F)$ is small compared to the differences between the hyperfine structure energy eigenvalues, legitimizing

the use of perturbation theory.

Approximate value of FORT potential depth

An order-of-magnitude calculation of $\Delta E(F, m_F)$ may be performed by simplifying the ^{87}Rb internal state structure, taking into account only two levels $5S_{1/2}$ and $5P_{3/2}$ (D2 transition). Since ΔE of the $5S_{1/2}$ state is the potential experienced by the atom, we can calculate ΔE by deriving the potential from the scattering force of FORT photons when the FORT light off-resonantly drives the D2 transition. Without using perturbation theory, one may derive [16] the photon scattering rate R_{scatt} and consequently the force is given by $\vec{F}_{scatt} = \hbar\vec{k} \cdot R_{scatt}$ where \vec{k} is the FORT wavevector. The potential U_0 is obtained by solving $\vec{F}_{scatt} = -\nabla U_0$, giving:

$$U_0 = \frac{\hbar\Gamma}{8} \frac{\Gamma}{\delta} \frac{I}{I_{sat}} \quad (\text{A.1})$$

where:

- Γ : D2 transition linewidth = $2\pi \cdot 6$ MHz
- δ : FORT frequency detuning from the D2 transition
- I_{sat} : Saturation intensity of the $|5S_{1/2}, F = 2, m_F = 2\rangle$ to $|5P_{3/2}, F' = 3, m'_F = 3\rangle$ σ^+ transition.
- I : Intensity of our FORT beam at the focus = $3 \times 10^8 I_{sat}$

For our FORT parameters (see Section 2.1) we obtain $|U_0| = 19$ MHz < 72 MHz, which is the minimum hyperfine frequency separation in the $5S_{1/2}$

and $5P_{3/2}$ manifolds (see fig A.1). Since typical hyperfine frequency separations within the $5S_{1/2}$, $5P_{1/2}$ and $5P_{3/2}$ manifolds are about hundreds of Megahertz, we are satisfied that the FORT could be treated as a perturbation to the unperturbed Hamiltonian of the free atom.

Stark shift formula

We thus continue with the perturbative treatment of FORT Hamiltonian. Under the dipole approximation, for a left-hand circularly polarised FORT used in our experiment, H_I could be re-written as:

$$\begin{aligned}
H_I(t) &= -\vec{d} \cdot \vec{E}(t) \\
&= -\vec{d} \cdot \frac{E_0}{\sqrt{2}} [\cos(\omega t)\hat{x} + \sin(\omega t)\hat{y}] \\
&= -\frac{E_0}{2}\hat{d}_{-1}e^{i\omega t} + \frac{eE_0}{2}\hat{d}_{+1}e^{-i\omega t} \\
&= V_+(\vec{d})e^{-i\omega t} + V_-(\vec{d})e^{i\omega t}
\end{aligned} \tag{A.2}$$

where $\vec{E}(t)$ is the time-dependent electric field in the FORT with a field amplitude $E_0(\vec{r})$. The position-dependence of E_0 has been suppressed in Equation A.2 for brevity. The dipole moment operator is given by $\vec{d} = (\hat{d}_x, \hat{d}_y, \hat{d}_z)$ for components in the x, y, z axis respectively. The following notations are

useful in this section:

$$\begin{aligned}
\hat{d}_{\pm 1} &= \frac{\mp(\hat{d}_x \pm i\hat{d}_y)}{\sqrt{2}} \\
\hat{d}_0 &= \hat{d}_z \\
V_{\pm}(\vec{d}) &= \pm \frac{E_0}{2} \hat{d}_{\pm 1}
\end{aligned}
\tag{A.3}$$

It could be evaluated that for a:

$$\begin{aligned}
\text{right-hand circularly polarised trap: } V_{\pm}(\vec{r}) &= \mp \frac{E_0}{2} \hat{d}_{\mp 1} \\
\text{linearly polarised trap: } V_+(\vec{d}) &= V_-(\vec{d}) = -\frac{E_0}{2} \hat{d}_0
\end{aligned}
\tag{A.4}$$

One finds from the derivation of [39] that the AC Stark shift of the $|F, m_F\rangle$ state due to the interaction Hamiltonian H_I may be written as:

$$\Delta E(F, m_F) \approx \sum_{F', m_{F'}} \left\{ \frac{|\langle F, m_F | V_-(\vec{d}) | F', m_{F'} \rangle|^2}{\hbar(\omega_F - \omega_{F'} + \omega)} + \frac{|\langle F, m_F | V_+(\vec{d}) | F', m_{F'} \rangle|^2}{\hbar(\omega_F - \omega_{F'} - \omega)} \right\},
\tag{A.5}$$

where $\hbar\omega_{F, F'}$ refer to the unperturbed energies. The m_F quantum numbers are suppressed as it is assumed that the magnetic sublevels are degenerate when unperturbed.

Equation A.5 contains the following matrix elements which can be reduced to a Wigner-3j, Wigner-6j and a reduced matrix element, by the

Wigner-Eckart theorem [40]:

$$\begin{aligned} \langle F, m_F | \hat{d}_q | F', m_{F'} \rangle &= \langle J || \vec{d} || J' \rangle (-1)^{J+I+m_F} \sqrt{(2F+1)(2F'+1)} \\ &\times \begin{pmatrix} F' & 1 & F \\ m_{F'} & q & -m_F \end{pmatrix}_{3j} \begin{pmatrix} J & J' & 1 \\ F' & F & I \end{pmatrix}_{6j} \end{aligned} \quad (\text{A.6})$$

$$= \langle J || \vec{d} || J' \rangle C_{F, m_{F'}, F, m_{F'}, J, J', I} \quad (\text{A.7})$$

where J, J' are the fine-structure angular momentum quantum numbers and I the nuclear angular momentum quantum number.

The reduced dipole matrix element may be obtained [41] from the spontaneous radiative lifetime τ of the relevant D1 ($J = 1/2, J' = 3/2$) or D2 ($J = 1/2, J' = 1/2$) line:

$$\frac{1}{\tau} = \frac{\omega_0^3}{3\pi\epsilon_0\hbar c^3} \frac{2J+1}{2J'+1} |\langle J || \vec{d} || J' \rangle|^2, \quad (\text{A.8})$$

with $\omega_0 = |\omega_{J'} - \omega_J|$. Note that, $|\langle J || \vec{d} || J' \rangle|^2 = |\langle J' || \vec{d} || J \rangle|^2$ in the above equations but J' in Equation A.8 should be that of the higher energy state.

According to Equation A.8, calculation of Equation A.5 requires knowledge of the lifetimes τ of all allowed dipole transitions connecting to the $|F, m_F\rangle$ state. While τ of transitions that concern the states within the $5S_{1/2}$ manifold is relatively well known, it is not so for those in the $5P_{3/2}$ manifold. Furthermore, values for τ available on existing atomic line databases [42, 43] are incompatible.

Tey [1] circumvented the former problem by assuming that the reduced dipole matrix elements of transitions between the higher energy states to the

$5P_{3/2}$ sublevels are 0.1 to 0.01 that of those concerning the D2 or D1 transitions. Fortunately, the inaccuracies in values of the reduced matrix element $|\langle J || \vec{d} || J' \rangle|^2$ in Equation A.6 do not change the ratio $\Delta E(F, m_F) / \Delta E(F, m'_F)$, so we still have an idea how energy levels are shifted relative to one another. This is because the ratio of magnitudes of $\langle F, m_F | \hat{d}_q | F', m_{F'} \rangle$ between adjacent m_F sublevels depend only on $C_{F, m_{F'}, F, m_{F'}, J, J', I}$ – levels having the same F quantum number have the same value of $|\langle J || \vec{d} || J' \rangle|^2$. Consequently, the ratio of $\Delta E(F, m_F)$ between adjacent m_F sublevels within the same hyperfine structure is independent of $|\langle J || \vec{d} || J' \rangle|^2$.

FORT polarisation

Figure 2.3 shows the calculated AC Stark shift [1] of the ($5S_{1/2}, F = 2$) and ($5P_{3/2}, F' = 3$) hyperfine states of ^{87}Rb under influence of a left-hand circular FORT where the FORT has maximum intensity. The calculated energy shift of the sublevels within the $5S_{1/2}$ hyperfine manifold is illustrated to be about $-\hbar \cdot 27 \text{ MHz} = -U_0$. In contrast, for a linearly polarised FORT, the Stark shift formula Equation A.5 contains elements $|\langle F, m_F | \hat{d}_0 | F', m_{F'} \rangle|^2$ which can be shown to be invariant under exchange of $m_F \leftrightarrow -m_F$. Consequently, the light shifts for $|F, m_F\rangle$ and $|F, -m_F\rangle$ are equivalent, and one cannot arrive at a non-degenerate Zeeman sublevel structure.

Selecting the FORT polarisation to be **left-hand-circular**, we induce non-degenerate Zeeman sublevel splitting, defining the z-axis as the quantisation axis. Further sublevel splitting is achieved by applying a DC biased magnetic field along the positive-z direction. In this case the Zeeman and AC Stark shifts have the same sign on the Zeeman sublevels of ($5S_{1/2}, F = 2$).

Spatial profile of FORT potential

It is clear from Equations A.5 and A.4 that $\Delta E(F, m_F)$ is directly proportional to $|E_0|^2$ and consequently, the intensity. For our FORT, the intensity distribution is Gaussian. Thus if the energy shift of $|F, m_F\rangle$ at the smallest waist of the FORT at position $(\rho, z) = (0, 0)$ is $\Delta E(F, m_F)_0$, then the energy shift at some position (ρ, z) is given by:

$$\Delta E(F, m_F)_{\rho, z} = \frac{\Delta E(F, m_F)_0}{(1 + z^2/z_R^2)} \exp \left[-\frac{2\rho^2}{w_D^2(1 + z^2/z_R^2)} \right] \quad (\text{A.9})$$

where $w_D = 1.56 \mu\text{m}$ is the smallest waist of the FORT and $z_R = \pi w_D^2/\lambda$ the FORT Rayleigh length. As the ^{87}Rb atom remains in the $5S_{1/2}$ ground state most of the time in the FORT, the energy shifts of the $|F, m_F\rangle$ states in this manifold determine its potential energy $U(\rho, z)$. For the left-hand circularly polarised FORT used in our experiment, it was estimated [2] that

$$U(\rho, z) = -\frac{U_0}{(1 + z^2/z_R^2)} \exp \left[-\frac{2\rho^2}{w_D^2(1 + z^2/z_R^2)} \right], \quad (\text{A.10})$$

where $\Delta E(5S_{1/2}, F = 1, m_F = 0) = \Delta E(5S_{1/2}, F = 2, m_F = 0) = -U_0$.

A.2.2 Trap Frequencies

Under paraxial approximation, an atom in a focused Gaussian intensity profile dipole trap would have the spatial distribution described by Equation A.10. If the mean kinetic energy of the atom ¹ is much smaller than the

¹There is only one atom in our FORT. The temperature here reflects the statistical average of the atomic kinetic energy in the FORT.

potential depth U_0 , the atom is localised near the bottom of the potential (verified in Chapter 3). In this case, the FORT potential can be approximated by a harmonic potential:

$$U(\rho, z) \approx -U_0 \left[1 - 2 \left(\frac{\rho}{w_D} \right)^2 - \left(\frac{z}{z_R} \right)^2 \right] \quad (\text{A.11})$$

$$= -U_0 + \frac{1}{2} m \omega_\rho \rho^2 + \frac{1}{2} m \omega_z z^2 \quad (\text{A.12})$$

where:

1. transverse oscillation frequency: $\omega_\rho = (4U_0/mw_D^2)^{1/2} = 2\pi \cdot 80 \text{ kHz}$
2. longitudinal oscillation frequency: $\omega_z = (2U_0/mz_R^2)^{1/2} = 2\pi \cdot 13 \text{ kHz}$
3. The mass of the ^{87}Rb atom is given by m .

A.2.3 FORT Scattering Rate

The left-hand circularly polarised FORT ($\lambda = 980 \text{ nm}$) off-resonantly drives the σ^+ transitions of the ^{87}Rb atom. Since the FORT is far-off detuned from both the D1 (795 nm) and D2 (780 nm) transitions, we expect the FORT photon scattering rate Γ_{sc} to be negligible. For a beam at FORT frequency ω off-resonant to a two-level transition between $|i\rangle$ and $|f\rangle$ at resonant frequency ω_{res} and having a spontaneous emission rate of Γ [16],

$$\Gamma_{sc} = \frac{3\pi c^2}{2\hbar\omega_{res}^3} \left(\frac{\omega}{\omega_{res}} \right)^3 \left(\frac{\Gamma}{\omega_{res} - \omega} + \frac{\Gamma}{\omega_{res} + \omega} \right) \quad (\text{A.13})$$

where Γ has an explicit position-dependence due to the position-dependence of the FORT intensity $I(\vec{r})$ as seen from $\Gamma(\vec{r}) = \frac{\omega_{res}^3}{3\pi\epsilon_0\hbar c^3} |\langle f|\mu|i\rangle|^2 I(\vec{r})$. While

several σ^+ transitions are possible between the hyperfine manifolds of $5S_{1/2}$ and $5P_{3/2}$ (D2), and also between the hyperfine manifolds of $5S_{1/2}$ and $5P_{1/2}$ (D1), we only take into account one particular σ^+ transition $|i\rangle = |5S_{1/2}, F = 2, m_F = 2\rangle \rightarrow |f\rangle = |5P_{3/2}, F' = 3, m'_F = 3\rangle$ for the purpose of calculating Γ_{sc} . Reason being that the amplitude for this transition is the only value available to us [29]. With our FORT parameters $\Gamma_{sc}(\vec{r} = \vec{0}) \approx 6 \text{ s}^{-1}$, we estimate a heating rate of $\hbar^2|\vec{k}|^2/(2m) \cdot \Gamma_{sc} = h \cdot 41 \text{ kJ s}^{-1}$. The wavevector of the FORT light was represented by \vec{k} , and m refers to the mass of the ^{87}Rb atom.

Within one period of the oscillation in the transverse direction $\tau_\rho = 2\pi/\omega_\rho = 12.5 \text{ }\mu\text{s}$, the atom gains an energy of $41h \cdot 12.5 \times 10^{-6} \approx 3\hbar \ll \hbar\omega_\rho$ by scattering FORT photons. Thus it is extremely unlikely that the atom gains a vibrational quanta of the transverse harmonic potential. The same analysis for the trap in the longitudinal harmonic potential yields the same conclusion. Thus the heating effects of the atom by the FORT can be neglected and the potential created by the FORT is therefore conservative.

A.3 Average vibrational quantum number in FORT

We have found in Section A.2.2 that the FORT potential is approximately harmonic for small excursions (ρ, z) away from the centre. Over many realisations of similarly trapped and Doppler cooled single atoms, one may assign to this ensemble an average weight for the occurrence of the Fock state

$|n_x, n_y, n_z\rangle$ in the three-dimensional harmonic potential.

In considering the ensemble, it is appropriate to characterise the vibrational state with a density matrix $\hat{\rho}$ with zero off-diagonal elements. This corresponds to maximum ignorance and therefore maximum entropy [44]. Thus the density matrix describes a mixed state, not a pure state. The diagonal elements correspond to the average occurrence of all possible Fock states in the ensemble. It can be shown [3] that for an ensemble of similarly trapped and Doppler cooled single atoms, the total energy of a single atom follows a Maxwell-Boltzmann distribution characterised by an ensemble ‘temperature’ T such that $\hat{\rho} = \hat{\rho}_{th} = e^{-\beta\hat{H}_{osc}}/Z$ where $\beta = k_B T$. The partition function is given by $Z = Tr[e^{-\beta\hat{H}_{osc}}]$, where $\hat{H}_{osc} = \hbar \sum_{j=x,y,z} \omega_j \hat{a}_j^\dagger \hat{a}_j$ is the Hamiltonian of the harmonic potential. We have determined in Chapter 3 that $T = 35(1) \mu\text{K}$.

To evaluate the average vibrational quantum number for say, the x-axis harmonic potential, we compute $\bar{n}_x = Tr[\hat{N}_x \hat{\rho}_{th}]$. The number operator is $\hat{N}_x = \hat{a}_x^\dagger \hat{a}_x$, where the creation and annihilation operators for a vibrational quanta in the harmonic potential along the x-axis are \hat{a}_x^\dagger and \hat{a}_x respectively. We remind ourselves that for a three-dimensional harmonic potential, the Hamiltonians \hat{H}_x, \hat{H}_y and \hat{H}_z commute with one another. Therefore it is sufficient to calculate

$$\bar{n}_x = Tr_x[\hat{N}_x \hat{\rho}_x]$$

where the trace is performed only for the range of Fock states which could

be bounded within the x-axis harmonic potential. Here,

$$\hat{\rho}_x = e^{-\beta\hbar\omega_x\hat{a}_x^\dagger\hat{a}_x}/Z_x$$

where

$$Z_x = \text{Tr}_x \left[e^{-\beta\hbar\omega_x\hat{a}_x^\dagger\hat{a}_x} \right] = \sum_{n_x=0}^{n_x^{max}} e^{-\beta\hbar\omega_x n_x} = \frac{1 - e^{-\beta\hbar\omega_x(n_x^{max}+1)}}{1 - e^{-\beta\hbar\omega_x}}$$

where $n_x^{max} \approx U_0/(\hbar\omega_x) = 337$, which is the maximum vibrational quantum number n_x that can be bounded by the x-axis harmonic potential. Evaluating

$$\bar{n}_x = \frac{1}{Z_x} \sum_{n_x}^{n_x^{max}} n_x e^{-\beta\hbar\omega_x n_x}$$

we obtain $\bar{n}_x = \bar{n}_y = \bar{n}_\rho = 8.6$ (recall that the transverse oscillation frequencies are equal $\omega_x = \omega_y = \omega_\rho$). Repeating the analysis for the z-axis harmonic oscillator we have $\bar{n}_z = 55.6$.

A.4 Two-photon stimulated Raman transitions and motional state coupling

In Section 4.1.2 we presented the sideband-resolved Raman cooling scheme involving a two-photon Raman transition driving a three-level atom in the FORT initially in the combined internal-vibrational state vector $|\uparrow, n_x\rangle$ to the final state $|\downarrow, n_x - 1\rangle$. Figure 4.1 illustrates the Raman cooling transition: Raman beams α and β create an effective two-level coupling of the above-

mentioned states by being off-resonant to a third level $|e\rangle$ by Δ_R , such that $|e\rangle$ is negligibly occupied at all times. By adjusting the frequency detuning of the Raman beams $\omega_\beta - \omega_\alpha = \omega_0 + \delta_\omega$ such that $\delta_\omega = \omega_x$, the $\Delta n_x = -1$ transition is driven, removing one phonon from the atom. Here, the separation between the internal states $|\uparrow\rangle$ and $|\downarrow\rangle$ is given by ω_0 .

General discussion of the theory behind sideband-resolved Raman cooling in one dimension of an atom confined in a harmonic potential can be found in [30]. Here we consolidate the formulae and assumptions which we use to predict the Rabi frequency of the cooling transition of an atom initially in its internal and vibrational state $|\uparrow, n_x, n_y, n_z\rangle$, but subject to a two-photon Raman transition transferring population from this internal state to $|\downarrow, N_x, N_y, N_z\rangle$ such that the vibrational quanta in more than one dimension is altered by the Raman transition. We begin with the Hamiltonian of a three-level atom in a harmonic trap:

$$\begin{aligned}\hat{H}_0 &= \hat{H}_{internal} + \hat{H}_{osc} \\ &= \hbar \sum_{m \in \{\downarrow, \uparrow, e\}} \omega_m |m\rangle \langle m| + \hbar \sum_{j=x,y,z} \omega_j \hat{a}_j^\dagger \hat{a}_j\end{aligned}\quad (\text{A.14})$$

where:

1. $\hat{H}_{internal}$ is the internal electronic state Hamiltonian with eigenvalues $\hbar\omega_1, \hbar\omega_2, \hbar\omega_3$ ($\omega_1 < \omega_2 < \omega_3$) corresponding to the internal eigenstates $|\downarrow\rangle, |\uparrow\rangle, |e\rangle$ respectively. The frequency separation between $|\uparrow\rangle$ and $|\downarrow\rangle$ is given by $\omega_0 = \omega_2 - \omega_1$.
2. \hat{H}_{osc} is the harmonic oscillator Hamiltonian induced by the FORT, with

oscillation frequency in the j -th axis given by ω_j . The creation and annihilation operators of vibrational quanta for the harmonic potential in the j -th axis are \hat{a}_j^\dagger and \hat{a}_j respectively.

When the atom is subjected to two Raman beams α and β with electric fields given by $\vec{E}_l \cos(\vec{k}_l \cdot \vec{r} - \omega_l t + \phi_l)$ where $l \in \{\alpha, \beta\}$, an additional Hamiltonian is introduced:

$$\begin{aligned} \hat{H}' &= -\vec{d} \cdot \sum_{l=\alpha}^{\beta} \vec{E}_l \cos(\vec{k}_l \cdot \vec{r} - \omega_l t + \phi_l) \\ &= -\hbar \sum_{l=\alpha}^{\beta} \hat{\sigma}_x^l \left(g_l e^{i(\vec{k}_l \cdot \vec{r} - \omega_l t)} + c.c \right) \end{aligned} \quad (\text{A.15})$$

where

1. \vec{d} is the electric dipole moment operator that operates exclusively on the internal state subspace.
2. \vec{r} the position operator of the atom.
3. $g_\alpha = e^{i\phi_\alpha} \langle e | \vec{d} \cdot \vec{E}_\alpha | \uparrow \rangle / (2\hbar)$ and $g_\beta = e^{i\phi_\beta} \langle e | \vec{d} \cdot \vec{E}_\beta | \downarrow \rangle / (2\hbar)$ are half the single-photon Rabi frequency of the α and β beams respectively, under the Rotating Wave Approximation (RWA).²
4. $\hat{\sigma}_x^l$ is analogous to the Pauli spin-flip operator, where the subscript x has no reference to the coordinate x of the atom but is rather reminiscent

²From [16]: For a two-level system between $|e\rangle$ and $|\uparrow\rangle$ mediated by a single field $\vec{E}_\alpha \cos(\vec{k}_\alpha \cdot \vec{r} - \omega_\alpha t + \phi_\alpha)$, the Rabi frequency is $\Omega_\alpha = \frac{\langle e | \vec{d} \cdot \vec{E}_\alpha | \uparrow \rangle}{\hbar}$ such that the population in $|e\rangle$ calculated assuming RWA is $|c_e(t)|^2 = \sin^2(\frac{\Omega t}{2})$. A population inversion is achieved at $\Omega t = \pi$.

of how for a spin-1/2 system, an up-spin in the z -direction can be ‘flipped’ to a down-spin by the Pauli operator $\hat{\sigma}_x$. In the experiment of Section 4.3, the Raman beams used to coherently transfer population from $|\uparrow\rangle$ to $|\downarrow\rangle$ had polarisations such that Raman beam α only off-resonantly couples states $|\uparrow\rangle$ and $|e\rangle$ while the coupling for Raman beam β is between $|\downarrow\rangle$ and $|e\rangle$. Thus we have $\hat{\sigma}_x^\alpha = |e\rangle\langle\uparrow| + |\uparrow\rangle\langle e|$ and $\hat{\sigma}_x^\beta = |e\rangle\langle\downarrow| + |\downarrow\rangle\langle e|$.

Transformation of \hat{H}' to the interaction picture results in a simple looking formula:

$$i\hbar\frac{\partial}{\partial t}|\Psi(t)\rangle_I = \hat{H}'_{int}|\Psi(t)\rangle_I \quad (\text{A.16})$$

where $\hat{H}'_{int} = \hat{U}_0^\dagger(t)\hat{H}'\hat{U}_0(t)$ is the ‘interaction Hamiltonian’. The transformed state vector is:

$$|\Psi(t)\rangle_I = \sum_{m \in \{\downarrow, \uparrow, e\}, n_x, n_y, n_z \in [0, +\infty)} c_{m, n_x, n_y, n_z}(t) |m, n_x, n_y, n_z\rangle_I = \sum_{m, \vec{n}} c_{m, \vec{n}}(t) |m, \vec{n}\rangle_I$$

such that $|\Psi(t)\rangle_I = \hat{U}_0^\dagger(t)|\Psi(t)\rangle$, where the state vector in the Schrödinger picture is given by $|\Psi(t)\rangle$. The time evolution operator in the steady state is $\hat{U}_0(t) = e^{-i\hat{H}_0 t/\hbar}$. To represent the number state of the 3D harmonic oscillator $|n_x, n_y, n_z\rangle_I$, we use a shorthand notation $|\vec{n}\rangle_I$. For succinctness however, the subscript I shall be omitted from the state vectors in the interaction picture in the following equations.

It can be inferred from the work of Deslauriers. L [30] that after applying RWA on terms oscillating at twice the optical frequencies ω_α or ω_β , and also by adiabatic elimination of the excited state $|e\rangle$, the amplitudes evolve as

in Equations A.18 and A.17. The adiabatic elimination procedure can be shown [30] to be justified when the detuning of both Raman beams from $|e\rangle$ is very large such that $1/\Omega_{Raman} \gg 1/\Delta_R$, where Ω_{Raman} is the frequency of the Rabi oscillation between $|\uparrow\rangle$ and $|\downarrow\rangle$.

$$\dot{c}_{\uparrow, \vec{N}} = i \frac{|g_\alpha|^2}{\Delta_R} c_{\uparrow, \vec{N}} + i \frac{g_\alpha^* g_\beta}{\Delta_R} \sum_{\vec{n}'} e^{i(\sum_j \omega_j (N_j - n'_j) - \delta_\omega)t} \langle \vec{N} | e^{i\Delta \vec{k} \cdot \vec{r}} | \vec{n}' \rangle c_{\downarrow, \vec{n}'} \quad (\text{A.17})$$

$$\dot{c}_{\downarrow, \vec{N}} = i \frac{|g_\beta|^2}{\Delta_R} c_{\downarrow, \vec{N}} + i \frac{g_\alpha g_\beta^*}{\Delta_R} \sum_{\vec{n}'} e^{i(\sum_j \omega_j (n'_j - N_j) + \delta_\omega)t} \langle \vec{N} | e^{-i\Delta \vec{k} \cdot \vec{r}} | \vec{n}' \rangle c_{\uparrow, \vec{n}'} \quad (\text{A.18})$$

The sum over \vec{n}' is taken over all possible vibrational quanta in the trap. We identify $\frac{|g_\alpha|^2}{\Delta_R}$ and $\frac{|g_\beta|^2}{\Delta_R}$ as the AC Stark shifts experienced by the $|\uparrow\rangle$ and $|\downarrow\rangle$ states respectively. The wavevector difference between the Raman beams is given by $\Delta \vec{k} = \vec{k}_\beta - \vec{k}_\alpha$.

The contribution from the AC Stark shift can be removed by performing the following transformation into another rotating frame given by:

$$c''_{\uparrow, \vec{N}} \rightarrow c_{\uparrow, \vec{N}} e^{i \frac{|g_\alpha|^2}{\Delta_R} t} \quad \text{and} \quad c''_{\downarrow, \vec{N}} \rightarrow c_{\downarrow, \vec{N}} e^{i \frac{|g_\beta|^2}{\Delta_R} t}$$

When the frequency detuning between the Raman beams $\omega_\beta - \omega_\alpha = \omega_0 + \delta_\omega$ is such that δ_ω is close to resonance between the particular $|\vec{n}\rangle \rightarrow |\vec{N}\rangle$ transition $\delta_\omega = \sum_{j \in \{x, y, z\}} \omega_j (N_j - n_j) + \Delta$, we can apply another rotating wave approximation resulting in a single stationary term in the sum over \vec{n}' ,

further simplifying the amplitudes to:

$$\dot{c}''_{\uparrow, \vec{N}} = i\Omega_{\vec{N}, \vec{n}} e^{-i\Delta t} c''_{\downarrow, \vec{n}} \quad (\text{A.19})$$

$$\dot{c}''_{\downarrow, \vec{N}} = i\Omega_{\vec{N}, \vec{n}}^* e^{i\Delta t} c''_{\uparrow, \vec{n}} \quad (\text{A.20})$$

Here, Δ refers to a small detuning of δ_ω from the resonance condition (see fig 4.1). We describe some important symbols:

1. We identify $\Omega_{\vec{N}, \vec{n}}$ as the generalised Rabi frequency driving the transition between $|\uparrow, \vec{n}\rangle$ and $|\downarrow, \vec{N}\rangle$

$$\begin{aligned} \Omega_{\vec{N}, \vec{n}} &= \frac{g_\alpha^* g_\beta}{\Delta_R} \langle N_x, N_y, N_z | e^{i(\Delta k_x \hat{x} + \Delta k_y \hat{y} + \Delta k_z \hat{z})} | n_x, n_y, n_z \rangle \\ &= \frac{g_\alpha^* g_\beta}{\Delta_R} \prod_{j=x,y,z} \langle N_j | e^{i\eta_j (\hat{a}_j^\dagger + \hat{a}_j)} | n_j \rangle \\ &= \Omega \prod_{j=x,y,z} \langle N_j | e^{i\eta_j (\hat{a}_j^\dagger + \hat{a}_j)} | n_j \rangle \end{aligned} \quad (\text{A.21})$$

We identify Ω as the two-photon ‘bare’ Rabi frequency, which is the frequency of the Rabi oscillation between $|\uparrow\rangle$ and $|\downarrow\rangle$ in the case where the atom is driven by the Raman beams but not confined within the harmonic trap:

$$\Omega = \frac{g_\alpha^* g_\beta}{\Delta_R} \quad (\text{A.22})$$

In the case when $\Delta \neq 0$, the Rabi oscillation frequency between the two levels is given instead by $\sqrt{\Omega_{\vec{N}, \vec{n}}^2 + \Delta^2}$.

2. The matrix element in Equation A.21 has an analytic solution [45]

which we can use to compute the numerical value for the Rabi frequency in Equation A.21. We suppress index j for succinctness:

$$\langle N | e^{i\eta(\hat{a}^\dagger + \hat{a})} | n' \rangle = e^{-\eta^2/2} \sqrt{\frac{N_<!}{N_>!}} \eta^{|N-n|} L_{N_<}^{|n-N|}(\eta^2) \quad (\text{A.23})$$

Where $N_<$ ($N_>$) denote the smaller (larger) of N and n . The associated Laguerre polynomial [45] is given by $L_{N_<}^{|n-N|}$.

3. The exponent η_j is known as the Lamb-Dicke parameter, which can be varied by adjusting the angle between the two Raman beams.

$$\eta_j = \Delta k_j j_0 \quad (j \in \{x, y, z\}) \quad (\text{A.24})$$

$$j_0 = \sqrt{\frac{\hbar}{2m\omega_j}} \text{ being the spread of the ground state wavefunction along harmonic trap axes } j \in \{x, y, z\} \quad (\text{A.25})$$

Discussion

1. **Resonance condition for a vibrational number changing transition:** From Equation A.21 we see that any motional state $|\vec{n}\rangle$ can be made to couple to $|\vec{N}\rangle$, given that the frequency detuning of the Raman beams $\omega_\beta - \omega_\alpha = \omega_0 + \delta_\omega$ is such that $\delta_\omega = \sum_j \omega_j (N_j - n_j) + \Delta$. For example, for a 3D harmonic trap with $\omega_x = \omega_y = 2\pi \cdot 80$ kHz and $\omega_z = 2\pi \cdot 13$ kHz, when the atom is subject to two Raman beams such that their wavevector difference $\Delta\vec{k}$ lies within the XZ plane, an atom initially in state $|\uparrow, 2, 2, 1\rangle$ could completely transfer population to $|\downarrow, 1, 2, 0\rangle$ under application of a Raman π -pulse $t_\pi = \pi/\Omega_{(1,2,0),(2,2,1)}$.

The frequency difference between the two Raman beams is given by:

$$\begin{aligned}
\omega_\beta - \omega_\alpha &= \omega_0 + \delta_\omega \\
&= \omega_0 + (2 - 1)\omega_x + (1 - 0)\omega_z. \\
&= \omega_0 + 2\pi \cdot 93 \text{ kHz}
\end{aligned} \tag{A.26}$$

where $\omega_0 = \omega_2 - \omega_1 =$ hyperfine ground state splitting (see figure 4.1). It is noteworthy that although $\delta_\omega = 93 \text{ kHz}$ also fulfills the frequency resonance condition for the $|\uparrow, 2, 2, 1\rangle \rightarrow |\downarrow, 2, 1, 0\rangle$ transition, this transition is forbidden as $\Delta\vec{k}$, in this example, lies in the XZ plane and has no component in the y-axis. In this beam geometry, the photons carry no momentum in the y direction and so it is impossible for the photons to cause the atomic vibrational state to change from $n_y = 2$ to $N_y = 1$. Mathematically, the term relevant to the y-axis in Equation A.21 is non-zero only when $N_y = n_y$:

$$\langle N_y | e^{i\Delta k_y \hat{y}} | n_y \rangle = \langle N_y | \mathbf{I} | n_y \rangle = \delta_{N_y, n_y} = \delta_{1, 2} = 0 \quad (\text{forbidden}) \tag{A.27}$$

2. Choice of two-photon Raman field over single-photon microwave

field: One can show from Equations A.21 and A.23 that for a $(\Delta n_x = -1, \Delta n_y = \Delta n_z = 0)$ transition, the Rabi frequency is given by

$$\Omega_{n_x-1, n_x} = \Omega \langle n_x - 1 | e^{i\eta_x (\hat{a}_x^\dagger + \hat{a}_x)} | n_x \rangle \approx \Omega \eta_x \sqrt{n_x} \tag{A.28}$$

for $\eta_x = (\Delta\vec{k} \cdot \hat{x})x_0 \ll 1$ which is often satisfied in quantum computing applications. It can be shown [30] that when the transition between $|\uparrow, n_x\rangle$ and $|\downarrow, n_x - 1\rangle$ is driven not by a two-photon transition but by a single-photon microwave field of wavevector \vec{k}_m , the Lamb-Dicke parameter becomes $\eta'_x = (\vec{k}_m \cdot \hat{x})x_0$. From Equation A.21 we see that the Rabi frequency is proportional to the Lamb-Dicke parameter. For counter-propagating Raman beams, $|\Delta\vec{k}| \approx 2k \approx 2\omega_\alpha/c$ (assuming $|\vec{k}_\alpha| \approx |\vec{k}_\beta| \approx k$). While for the microwave field, $k_m = \omega_m/c$. Since ω_α lies within the optical domain, while ω_m within the microwave domain, the former is typically about eight orders of magnitude larger than the latter, resulting in a much larger Lamb-Dicke parameter and Rabi frequency and consequently, smaller π -pulse timing for the transition. Thus the two-photon Raman transition is used as we require the cooling transition to be driven as fast as possible, given the limited coherence time of the atom.

Remarks

1. In order to effectively use the motional-electronic state coupling for sideband-resolved Raman cooling, we require that the coherence time t_C of the trapped atom to be much longer than t_π .
2. A large $\Delta_R \gg \Omega_{\vec{N}, \vec{n}}$ effectively decouples $|e\rangle$ and we have a closed two-level system. For any two-level system, the linewidth of a dipole transition can be shown to be inversely proportional to the duration of the Raman beam application time. Hence, to resolve all possible

transitions $t_\pi \gg \frac{1}{\omega_z/(2\pi)}$, where ω_z is the minimum frequency separation between any two resonance conditions.

3. The ^{87}Rb atom experiences a position-dependent FORT potential arising from position-dependent AC Stark shifts of the internal hyperfine ground state manifold of the $5S_{1/2}$ state. The internal states in figure 4.1 are dressed with vibrational energy levels of the confining potential. However, these dressed levels do not acquire a further position-dependent AC Stark shift, leading to position-dependent resonance conditions on δ_ω .

This is clearly demonstrated when we write the Hamiltonian of the harmonic potential given by:

$$\begin{aligned}\hat{H}_{osc} &= \sum_j \frac{\hat{p}_j^2}{2m} - U_0 \left[\mathbf{1} - 2 \left(\frac{\hat{\rho}}{w_D} \right)^2 - \left(\frac{\hat{z}}{z_R} \right)^2 \right] \\ &= \sum_j \frac{\hat{p}_j^2}{2m} - U_0 \cdot \mathbf{1} + \frac{1}{2} m \omega_\rho \hat{\rho}^2 + \frac{1}{2} m \omega_z \hat{z}^2\end{aligned}\quad (\text{A.29})$$

Where the terms in the square braces accounts for the position-dependent potential in the FORT. The maximum potential depth U_0 is at the FORT focus between the two aspheric lenses (see fig 2.1), where $(\rho, z) = (0, 0)$. The position-dependence of \hat{H}_{osc} represented by the position op-

erators in Equation A.29 is replaced by the number operator $\hat{a}_j^\dagger \hat{a}_j$:

$$\begin{aligned}
\hat{H}_{osc} &= -U_0 \cdot \mathbf{1} + \sum_{j \in x, y, z} \left(\frac{\hat{p}_j^2}{2m} + \frac{1}{2} m \omega_j \hat{j}^2 \right) \\
&= -U_0 \cdot \mathbf{1} + \hbar \sum_{j=x, y, z} \left(\omega_j \hat{a}_j^\dagger \hat{a}_j + \frac{1}{2} \right) \\
&\rightarrow \hbar \sum_{j=x, y, z} \omega_j \hat{a}_j^\dagger \hat{a}_j \tag{A.30}
\end{aligned}$$

From Equation A.30, we see that \hat{H}_{osc} , expressed in terms of the number operator $\hat{a}_j^\dagger \hat{a}_j$, does not contain any explicit dependence on the position operators \hat{j} . Hence, its eigenvalues, which are the energies of the dressed internal atomic states, are not position-dependent.